

1 Overview: Fusion of Radar Polarimetry and Numerical Atmospheric 2 Modelling Towards an Improved Understanding of Cloud and 3 Precipitation Processes

4 Silke Trömel^{1,2}, Clemens Simmer¹, Ulrich Blahak³, Armin Blanke¹, Florian Ewald⁴, Michael Frech⁵,
5 Mathias Gergely⁵, Martin Hagen⁴, Sabine Hörnig⁶, Tijana Janjic⁷, Heike Kalesse-Los⁶, Stefan Kneifel⁸,
6 Christoph Knotte^{7,9}, Jana Mendrok³, Manuel Moser^{10,4}, Gregor Köcher⁷, Kai Mühlbauer¹, Alexander
7 Myagkov¹¹, Velibor Pejic¹, Patric Seifert¹², Prabhakar Shrestha¹, Audrey Teisseire¹², Leonie von Terzi⁸,
8 Eleni Tetoni⁴, Teresa Vogl⁶, Christiane Voigt^{10,4}, Yuefei Zeng⁷, Tobias Zinner⁷, Johannes Quaas⁶

9 ¹Institute for Geosciences, Department of Meteorology, University of Bonn, Bonn, 53121, Germany

10 ²Laboratory for Clouds and Precipitation Exploration, Geoverbund ABC/J, Bonn, 53121, Germany

11 ³Deutscher Wetterdienst (DWD), Offenbach, 63067, Germany

12 ⁴Institute for Physics of the Atmosphere, DLR, Oberpfaffenhofen, 82234, Germany

13 ⁵Deutscher Wetterdienst (DWD), Observatorium Hohenpeißenberg, Hohenpeißenberg, 82383, Germany

14 ⁶Institute for Meteorology, Universität Leipzig, Leipzig, 04103, Germany

15 ⁷Meteorological Institute Munich, Ludwig-Maximilians-Universität München, 80333, Germany

16 ⁸Institute of Geophysics and Meteorology, University of Cologne, 50969, Germany

17 ⁹Faculty of Medicine, University of Augsburg, Augsburg, 86159 Germany

18 ¹⁰Institute for Physics of the Atmosphere, University Mainz, Mainz, 55099, Germany

19 ¹¹Radiometer Physics GmbH, Meckenheim, 53340, Germany

20 ¹²Leibniz Institute for Tropospheric Research (TROPOS), 04318 Leipzig, Germany

21
22
23 *Correspondence to:* Silke Trömel (silke.troemel@uni-bonn.de)

24 **Abstract.** Cloud and precipitation processes are still a main source of uncertainties in numerical weather prediction and climate
25 change projections. The Priority Program “Polarimetric Radar Observations meet Atmospheric Modelling (PROM)“, funded
26 by the German Research Foundation (Deutsche Forschungsgemeinschaft, DFG), is guided by the hypothesis that many
27 uncertainties relate to the lack of observations suitable to challenge the representation of cloud and precipitation processes in
28 atmospheric models. Such observations can, however, at present be provided e.g. by the recently installed dual-polarization
29 C-band weather radar network of the German national meteorological service in synergy with cloud radars and other
30 instruments at German supersites and similar national networks increasingly available worldwide. While polarimetric radars
31 potentially provide valuable in-cloud information e.g. on hydrometeor type, quantity, and microphysical cloud and
32 precipitation processes, and atmospheric models employ increasingly complex microphysical modules, considerable
33 knowledge gaps still exist in the interpretation of the observations and in the optimal microphysics model process formulations.

34 PROM is a coordinated interdisciplinary effort to increase the use of polarimetric radar observations in data assimilation, which
35 requires a thorough evaluation and improvement of parameterizations of moist processes in atmospheric models. As an
36 overview article of the inter-journal special issue “Fusion of radar polarimetry and numerical atmospheric modelling towards
37 an improved understanding of cloud and precipitation processes”, this article outlines the knowledge achieved in PROM during
38 the past two years and gives perspectives for the next four years.

39 **1 Introduction and Objectives of the priority program**

40 Among the main sources of uncertainty in the models used in numerical weather prediction (NWP) and climate change
41 projections are the parameterizations of cloud and precipitation processes (Bauer et al., 2015). A major part of these
42 uncertainties can be attributed to missing observations suitable to challenge the representation of cloud and precipitation
43 processes employed in atmospheric models. A wealth of new information on precipitation microphysics and generating
44 processes can be gained from observations from polarimetric weather radars and their synergistic analysis at different
45 frequencies. The dual-polarization upgrade of the United States National Weather Service (NWS) S-band Weather
46 Surveillance Radar 1988 Doppler (WSR-88D) network was completed in 2013. Germany finished upgrading its C-band
47 network to polarimetry in 2015 in parallel with other European countries. The synergistic exploitation of polarimetric
48 precipitation radars together with measurements from cloud radars and other instrumentation available at supersites and
49 research institutions enables for the first time a thorough evaluation and potential improvement of current microphysical
50 parameterizations based on detailed multi-frequency remote-sensing observations. Data assimilation merges observations and
51 models for state estimation as a prerequisite for prediction and can be seen as a smart interpolation between observations while
52 exploiting the physical consistency of atmospheric models as mathematical constraint.

53 Considerable knowledge gaps still exist, however, both in radar polarimetry and atmospheric models, which still impede the
54 full exploitation of the triangle between radar polarimetry, atmospheric models, and data assimilation and call for a coordinated
55 interdisciplinary effort. The German Research Foundation (Deutsche Forschungsgemeinschaft, DFG) responded to this call
56 and established the Priority Program “Polarimetric Radar Observations meet Atmospheric Modelling (PROM)”; its first 3-
57 year funding period began in 2019, which will be followed by a second funding period starting in 2022. PROM exploits the
58 synergy of polarimetric radar observations and state-of-the-art atmospheric models to better understand moist processes in the
59 atmosphere, and to improve their representation in climate- and weather prediction models. The overarching goal is to extend
60 our scientific understanding at the verges of the three disciplines, radar polarimetry – atmospheric models – data assimilation,
61 for better predictions of precipitating cloud systems. To approach this goal the initiators of PROM at the Universities of Bonn
62 and Leipzig in Germany identified the following five objectives (see also Trömel et al., 2018):

- 63 1) Exploitation of radar polarimetry for quantitative process detection in precipitating clouds and for model evaluation
64 including a quantitative analysis of polarimetric fingerprints and microphysical retrievals,
- 65 2) improvement of cloud and precipitation schemes in atmospheric models based on process fingerprints detectable in
66 polarimetric observations,
- 67 3) monitoring of the energy budget evolution due to phase changes in the cloudy, precipitating atmosphere for a better
68 understanding of its dynamics,
- 69 4) analyzing precipitation system by assimilation of polarimetric radar observations into atmospheric models for weather
70 forecasting, and
- 71 5) radar-based detection of the initiation of convection for the improvement of thunderstorm prediction.

72 In the first funding period, each of the 14 projects (see <https://www2.meteo.uni-bonn.de/spp2115>) distributed over Germany
73 contribute to at least one of these objectives. In most projects, a radar meteorologist works together with a modeller in order
74 to successfully combine expert knowledge from both research fields. This overview article of the ACP/AMT/GMD inter-
75 journal special issue entitled "Fusion of radar polarimetry and numerical atmospheric modelling towards an improved
76 understanding of cloud and precipitation processes" outlines methodologies developed and results achieved from a selection
77 of the projects during the past two years, and provides overall perspectives for the next four years. The paper is organized as
78 follows: Section 2 explains prevailing challenges in the representation of clouds in atmospheric models, while Sect. 3 provides
79 methodologies to extend our insight in the microphysics of clouds and precipitation by exploiting radar polarimetry. Section 4
80 addresses the fusion of numerical modelling and radar polarimetry via model evaluation either in radar observation space using
81 observation operators or using microphysical retrievals. First conclusions for improved model parameterizations and for a
82 better representation of model uncertainty in radar data assimilation are drawn. Section 5 provides a summary and perspectives
83 for the following years.

84 **2 Representation of clouds in atmospheric models**

85 The representation of cloud and precipitation processes in atmospheric models is a central challenge for NWP and climate
86 projections (e.g., Bauer et al., 2015; Forster et al., 2021), which also impacts offline hydrological models by modulating the
87 distribution of incoming solar radiation and precipitation and affecting the simulated hydrological processes such as
88 evapotranspiration, runoff, and groundwater depths (e.g., Shrestha, 2021). While the primitive equations provide a solid
89 theoretical basis for atmospheric model dynamics, the key diabatic processes that drive energetics and thus circulation, are
90 poorly resolved. Important diabatic processes are linked to cloud and precipitation microphysics acting at scales of micrometres
91 and turbulent processes ranging from several to hundreds of meters. While significant progress has been achieved by high-
92 resolution modelling at the coarser end of this range (e.g., Heinze et al., 2017; Stevens et al., 2020), the intricate and complex
93 microphysical processes still require parameterizations in any dynamic atmospheric model down to and including the scale of
94 direct numerical simulations (e.g., Mellado et al., 2009).

95 A key uncertainty in weather prediction and climate modelling results from the still-rudimentary representation of moist
96 processes and from the diabatic heating/cooling the models induce due to latent heat and their interaction with radiation. The
97 generation and interpretation of past and future climate states additionally has to consider changes in microphysical processes
98 due to anthropogenic aerosol acting, e.g., as cloud condensation nuclei and ice nucleating particles. For short-term weather
99 prediction, the location and evolution of convective events with lifetimes of hours or less are particularly challenging, while
100 relatively slow moving and frontal systems with lifetimes of days show reasonable predictability (Alifieri et al., 2012).

101 Atmospheric modelling in Germany has recently seen substantial advances both in terms of cloud-resolving simulations in
102 NWP mode and in the implementation of ice and mixed-phase precipitation formation processes. Traditionally, different model
103 systems were used for NWP and climate modelling, which were also both heavily used in academic research. The modelling
104 system for long-term climate integrations is the ECHAM model (Stevens et al., 2013). Since it was created by modifying
105 global forecast models developed by ECMWF (European Centre for Medium-Range Weather Forecasts), its name is a
106 combination of ECMWF and Hamburg, the place of development of its parameterization package. The COSMO model,
107 however, was operated at horizontal resolutions down to 2.8 km and used for NWP and reanalysis studies. Both model families
108 are currently being replaced by the ICOSahedral Nonhydrostatic (ICON) modelling framework (Zängl et al., 2015) jointly
109 developed by the Max-Planck Institute for Meteorology and the German national meteorological service (Deutscher
110 Wetterdienst, DWD). Its climate version (the ICON general circulation model, ICON GCM) inherited its physics package
111 from the ECHAM model, and the NWP version incorporated the one from the COSMO model. A third version largely based
112 on the COSMO physics package was developed for higher resolutions (Dipankar et al., 2015) and employs a large-eddy
113 turbulence scheme (ICON-LEM). The latter is able to operate on large domains (Heinze et al., 2017; Stevens et al., 2020) and
114 includes aerosol-cloud interactions (Costa-Surós et al., 2020). In PROM primarily the three ICON model variants (ICON-
115 LEM, ICON-NWP, and ICON-A/GCM) are used.

116 In most atmospheric models, cloud and precipitation microphysical processes are represented by bulk microphysical schemes
117 that distinguish between different hydrometeor classes and include their specific masses as prognostic variables while their
118 size distributions are parameterized (the ICON model considered here uses the scheme by Seifert and Beheng, 2006).
119 Computationally much more demanding are so-called spectral-bin microphysics schemes (Khain et al., 2015), which evolve
120 cloud- and precipitation particle size distributions discretized into size-interval bins. An example is the Hebrew University
121 Cloud Model (HUCM) created by Khain et al. (2005) that treats both liquid and much more intricate (since ice may occur in
122 various shapes and densities) ice crystal distributions. The model is employed by some of the PROM projects in addition to
123 the liquid-only bin-microphysics model by Simmel et al. (2015) extended to the ice phase based on the scheme by Hashino
124 and Tripoli (2007). For the simulation of the evolution of specific air volumes a Lagrangian particle model (McSnow; Brdar
125 and Seifert, 2018) is used in PROM, that models ice and mixed-phase microphysical processes such as depositional growth,
126 aggregation, riming, secondary ice generation, and melting closer to the real processes than bulk formulations. Microphysical

127 processes including radiation-particle interactions obviously depend on particle shape; thus, the evolution of shapes in particle
128 models – and their signatures in radar observations – is instrumental for a full understanding and adequate representation of
129 the microphysical processes in models. Advanced microphysical parameterizations such as spectral-bin or Lagrangian particle
130 schemes are relevant for cloud-resolving models and exploited in PROM for the development and improvement of bulk
131 parameterizations. Scientific questions about global climate require long model integrations and thus coarse spatial resolutions
132 due to computing time constraints. At these resolutions (usually of order of $100 \times 100 \text{ km}^2$ in the horizontal), fractional
133 cloudiness needs to be considered when the grid-box mean relative humidity is below 100%, which requires parameterizations
134 of subgrid-scale variability in relative humidity. Here, PROM builds on assumptions employed in the global ICON model
135 (ICON GCM) to predict fractional cloudiness (e.g., Quaas, 2012).

136 **3 Observational insights from polarimetric radar observations and challenges**

137 DWD operates 17 state-of-the-art polarimetric Doppler C-band weather radars which provide a 3-D sampling of precipitating
138 particles above Germany every five minutes. Together with their Doppler information, radars are the backbone for precipitation
139 and nowcasting products for all meteorological services. Although precipitation monitoring is still the most widespread
140 application of weather radars, their upgrade to polarimetry worldwide not only improves precipitation estimates; their
141 observations are also increasingly exploited for the evaluation and improvement of the representation of cloud- and
142 precipitation processes in atmospheric models (e.g., Gao et al., 2011; Jung et al., 2012; You et al., 2020; Wang et al., 2020).
143 Additional observations from cloud radars available at so-called supersites (in Germany e.g., the Jülich Observatory for Cloud
144 Evolution – Core Facility; JOYCE-CF; Löhnert et al., 2015; <http://www.cpex-lab.de>), universities, and research facilities (e.g.
145 the Leipzig Aerosol and Cloud Remote Observations System; LACROS; Bühl et al., 2013) open opportunities to inform and
146 improve atmospheric models. The use of shorter wavelengths of cloud radars shifts the sensitivity of the observations towards
147 smaller particles and partly increases the magnitude of the received polarimetric signals (e.g. K_{DP} – the differential phase shift
148 between horizontal and vertical polarization per distance called specific differential phase – scales with λ^{-1}), which allows for
149 more detailed studies of ice and cloud microphysics. Polarimetric and multi-frequency radar observations allow for a more
150 granular look at microphysical processes and provide a great data base for model evaluation, the improvement of microphysical
151 parameterizations, and data assimilation, and thus have the potential to significantly improve both weather forecasts and
152 climate predictions.

153 **3.1 Multi-frequency and spectral polarimetry for ice and cloud microphysics**

154 The PROM-project *Understanding Ice Microphysical Processes by combining multi-frequency and spectral Radar*
155 *polarImetry aNd super-parTicle modelling (IMPRINT)* improves ice microphysical process understanding by using spectral
156 multi-frequency and radar polarimetric observations in combination with Monte-Carlo Lagrangian super-particle modeling
157 (Brdar and Seifert, 2018). Mid-latitude stratiform clouds, which occur frequently during winter time over JOYCE-CF, are the

158 main focus. Radar polarimetric variables are well known to be particularly sensitive to the presence of asymmetric ice particles
159 (e.g. Kumjian, 2013). Only recently, also polarimetric cloud radars operating at Ka or W-band are routinely available (Oue et
160 al., 2018; Myagkov et al., 2016; Bühl et al., 2016; Matrosov et al., 2012). Some polarimetric variables are wavelength
161 dependent (K_{DP} is inversely proportional to the wavelength), which provides enhanced sensitivity to ice particle concentration
162 at higher frequencies. Multi-frequency approaches are complementary to radar polarimetry as they are sensitive to larger ice
163 particles. Most commonly, the dual wavelength ratio (DWR), defined as the logarithmic difference of the effective reflectivity
164 Z_e at two frequencies, is used. When ice particles transition from Rayleigh into non-Rayleigh scattering from one wavelength
165 to a higher one, the DWR increases, which allows inferring the characteristic size of the underlying size distribution. The use
166 of three radar frequencies (e.g. X, Ka, W) extends the discernable size range; e.g. the DWR of the Ka-W combination saturates
167 for very large particles (Kneifel et al., 2015; Ori et al., 2021). The information content can be further extended when also the
168 Doppler spectral information is explored. The different fall velocities allow for the separation of different hydrometeors; the
169 high differential reflectivity (Z_{DR}) signal originating from small, slow falling ice crystals can be distinguished from the also
170 low Z_{DR} signal of faster falling snow aggregates, which usually dominate the total Z_{DR} . Only few studies used so far spectral
171 polarimetric observations for ice and snow microphysical studies (Luke et al., 2021; Oue et al., 2018; Pfitzenmayer et al.,
172 2018; Spek et al., 2008). The observations collected during the first multi-months winter campaign carried out at JOYCE-CF
173 as part of the IMPRINT project provide for the first time the opportunity to investigate both, polarimetry and multi-frequency
174 observations in the Doppler spectra space. An example is the analysis of the dendritic growth layer (DGL) illustrated in Fig. 1
175 for a snowfall event observed on 22 January 2019 at JOYCE-CF. Especially in the upper half of the cloud, Z_{DR} is enhanced
176 while K_{DP} values are low (Fig. 1b-c). Starting at the $-15\text{ }^\circ\text{C}$ isotherm, Z_{DR} sharply decreases and shows an anti-correlation with
177 the enhanced DWR (Fig. 1a) and K_{DP} values. These polarimetric signatures have been reported by previous studies (e.g.,
178 Moisseev et al., 2015 among others), and also the DWR increase below the $-15\text{ }^\circ\text{C}$ level resembles the examples shown in Oue
179 et al. (2018). Oue et al. (2018) concluded in agreement with findings in Moisseev et al. (2015), that an increasing concentration
180 of asymmetric aggregates is partly responsible for enhanced K_{DP} values because the number of small ice particles decrease due
181 to aggregation. The spectrally-resolved Z_{DR} (sZ_{DR} , Fig. 1e), however, reveals that high Z_{DR} -producing, slowly falling ice
182 particles are still present down to the $-5\text{ }^\circ\text{C}$ level. The spectrally resolved DWR (Fig. 1d) shows that the particles falling from
183 above into the DGL are already partly aggregated. At $-17\text{ }^\circ\text{C}$, the spectra are much wider and a new spectral mode appears
184 which is linked to the rapid sZ_{DR} increase (Fig. 1e). The new ice particle mode increases in Doppler velocity and $sDWR$ until
185 20 dB are reached. Unlike Z_{DR} , K_{DP} (Fig. 1c and f) remains at values between 1 and 2 deg km^{-1} down to the $-5\text{ }^\circ\text{C}$ level. A
186 possible explanation of the bimodal spectra - increased sZ_{DR} and K_{DP} - might be secondary ice processes such as collisional
187 fragmentation (Field et al., 2017). The few existing laboratory studies indicate that the number of fragments rapidly increases
188 at $-20\text{ }^\circ\text{C}$, reaching a maximum at $-17\text{ }^\circ\text{C}$ and decreasing again towards $-10\text{ }^\circ\text{C}$ (Takahashi et al., 1995; Takahashi, 2014). This
189 temperature dependence fits well to the observed radar signatures in the DGL, although the laboratory studies only considered
190 collisions of solid ice spheres. As we can exclude strongly rimed particles in the snowfall case shown in Fig. 1, fragile dendritic
191 structures growing on the surface of aggregates might be responsible, which precipitate into the DGL and might easily break

192 into smaller pieces during particle collisions (Fig. 1d). Monte-Carlo Lagrangian super-particle model (Brdar and Seifert, 2018)
193 simulations were recently extended in IMPRINT by a habit prediction scheme and a parameterization of ice collisional
194 fragmentation following Phillips et al. (2017). The role of ice fragmentation and other ice microphysical processes is currently
195 investigated with a radar observation operator for explaining the observed radar signatures of intense aggregation shown in
196 Fig. 1.

197
198 The PROM-project *Investigation of the initiation of convection and the evolution of precipitation using simulations and*
199 *polarimetric radar observations at C- and Ka-band (IcePolCKa)* combines observations of the C-band Polarization Diversity
200 Doppler Radar (POLDIRAD) at the German Aerospace Center (DLR), Oberpfaffenhofen, with those of the Ka-band,
201 Millimeter-wave cloud RADar of the Munich Aerosol Cloud Scanner (miraMACS) at Ludwig-Maximilians-Universität (LMU),
202 Munich. While IMPRINT combines triple-frequency zenith-pointing observations with spectral cloud radar polarimetry,
203 IcePolCKa explores the life cycle of convective precipitation with spatially separated weather and cloud radars in order to
204 quantify ice crystal properties in precipitation formation. The project focuses on ice particle growth and its role in precipitation
205 formation within convective cells. Coordinated Range-Height-Indicator (RHI, varying elevation at constant azimuth) scans
206 along the 23 km long cross-section between both radars allow to observe DWR (Fig. 2a) and Z_{DR} (Fig. 2b) fingerprints of
207 individual convective cells. While the deviation from Rayleigh scattering with increasing ice crystal size at the cloud radar
208 wavelength allows distinguishing regions dominated by aggregation from regions with depositional growth, the slanted
209 perspective of the weather radar helps to narrow down the aspect ratio of ice crystals. Although the DWR technique to infer
210 ice crystal size is well established (e.g. Kneifel et al., 2015), assumptions about the unknown ice crystal shape are necessary.
211 Here, simultaneous polarimetric measurements, like Z_{DR} , help to narrow down estimates of the average asphericity of ice
212 crystals and reduce ambiguities in retrieving ice crystal size and ice water content. IcePolCKa develops an algorithm, which
213 uses Z_H , Z_{DR} and DWR measurements from the two radars to retrieve IWC, the mean particle diameter D_m , and the aspect ratio
214 of ice crystals using a least-squares fit between measurements and T-matrix scattering simulations. The model of horizontally
215 aligned spheroids in combination with an effective medium approximation following Hogan et al (2012) is used to find the
216 simplest ice particle model which explains the multi-wavelength polarimetric measurements. The approach allows studying
217 the covariance of DWR and Z_{DR} while varying particle density, mean particle diameter D_m , and aspect ratio. More sophisticated
218 models, such as discrete dipole approximation (DDA) simulations of specific ice crystals, would require the knowledge of the
219 aspect ratio, and make it hard to identify ice shape collections along these free variables. The multi-wavelength polarimetric
220 measurements are also used as a benchmark for convective precipitation formation in NWP models, where cloud microphysics
221 introduce substantial uncertainty (e.g. Morrison et al., 2020; Xue et al., 2017). In IMPRINT simulated microphysical processes
222 in NWP models will be compared to fingerprints in radar observations: A nested WRF setup covering the overlap area of both
223 radars is used to simulate convective events with microphysical schemes of varying complexity while the Cloud-resolving
224 model Radar SIMulator (CR-SIM; Oue et al., 2020), produces synthetic radar observations, such as DWR (Fig. 2c) and Z_{DR}
225 (Fig. 2d). Fig. 2 illustrates that the Predicted Particle Properties (P3) scheme (Morrison and Milbrandt, 2015) is able to produce

226 DWR features of similar magnitude and variability compared to the observations, while a realistic ice particle asphericity is
227 still missing. IcePolCKa compiled over 30 convective days of polarimetric measurements and simulations with 5 different
228 schemes over a 2-year period, which is currently used to analyse how well these different microphysical schemes reproduce
229 the polarimetric observations. A cell-tracking algorithm (TINT; Fridlind et al., 2019) facilitates the comparison on a cell object
230 basis. Comparison of macrophysical cloud characteristics, such as echo top height or maximum cell reflectivity, show that the
231 model simulates too few weak and small-scale convective cells, independent of the microphysics scheme. In ongoing studies,
232 the P3 scheme seems to better represent radar signatures within the ice phase, while a spectral bin scheme tends to better
233 simulate radar signatures within rain, where all other schemes are not able to correctly reproduce observed Z_{DR} features.

234
235 The PROM-project *A seamless column of the precipitation process from mixed-phase clouds employing data from a*
236 *polarimetric C-band radar, a micro-rain radar and disdrometers (HydroColumn)* characterizes precipitation processes inside
237 a vertical atmospheric column by combining polarimetric Doppler weather radar observations with co-located measurements
238 from micro-rain radars, disdrometers and in-situ measurements, and by relating these observations to the large-scale
239 atmospheric thermodynamics derived from NWP models. To date, spectral analyses are mostly performed with cloud radars
240 operating at shorter wavelengths (see previous paragraphs or, e.g., Shupe et al., 2004; Verlinde et al., 2013; Kalesse et al.,
241 2016; Gehring et al., 2020; Li and Moisseev, 2020), but their implementation across the national C-band radar network offers
242 prospects for operational area-wide applications, e.g. the identification of dominant precipitation particle growth processes
243 such as aggregation or riming. While the operational DWD birdbath scan has so far been used primarily to monitor Z_{DR} (Frech
244 and Hubbert, 2020), *HydroColumn* now also exploits the Doppler spectra measured at C-band for the analysis of
245 microphysical process information. Fig. 3 shows quasi-vertical profiles (QVPs; Trömel et al., 2014; Ryzhkov et al., 2016) of
246 polarimetric variables and Doppler spectra from birdbath scans for a stratiform precipitation event monitored with the
247 Hohenpeißenberg C-band research radar (47.8014N, 11.0097E) of DWD together with in-situ particle images obtained by the
248 Falcon research aircraft from DLR during the BLUESKY campaign (Voigt et al., 2021) within the *POLICE* project
249 (Sect.4.2.1). In-situ measurements have been performed with the Cloud, Aerosol and Precipitation Probe CAPS (Kleine et al.,
250 2018) integrated in a wing station on the Falcon flying within a horizontal distance of about 20 km from the radar site and
251 within about ± 15 min of the radar measurements. The dendritic growth layer (DGL; Ryzhkov and Zrnica, 2019) centered around
252 -15 °C is characterized by Z_{DR} maxima of ~ 1 dB and K_{DP} of ~ 0.2 deg km⁻¹, and a strong Z_H increase towards lower levels
253 (Fig. 3a). Particle images collected at temperatures below about -15 °C indicate mostly small irregular ice particles with the
254 number of larger particles increasing toward -15 °C (see levels L1 and L2 in Fig. 3c), and further down also reveal dendrites
255 and plates (L3, L4). In general, aggregation and riming become highly effective particle growth mechanisms at temperatures
256 around -7 °C (Libbrecht, 2005), and both processes result in a reduction of Z_{DR} (Fig. 3a). The vertically pointing Doppler
257 measurements can be used here to gain a deeper insight into the particle growth process. In this case study, the Doppler
258 measurements illustrated in Fig. 3b indicate typical ice-particle fall speeds increasing to about 2 m s⁻¹ just above the melting
259 layer and thus suggest a transition from predominantly aggregates to moderately rimed particles based on the relationship

260 between Doppler velocity and riming degree found by Kneifel and Moisseev (2020). This conclusion is supported by the
261 corresponding in-situ images showing increasing riming of polycrystals and aggregates toward the melting layer (L6). The
262 analysis confirms the benefit of interpreting radar signatures from polarimetric weather radar observations in combination with
263 vertically pointing Doppler radar measurements, which was previously pointed out for higher-frequency cloud research radars
264 (Oue et al., 2018; Kumjian et al., 2020). This novel application of radar spectral analysis to vertically-pointing operational
265 weather radar scans may provide a more detailed view into intense precipitation events, such as hailstorms, where the use of
266 cloud radars is severely limited due to the strong attenuation at high radar frequencies.

267 **3.2. Anthropogenic modifications of precipitation microphysics**

268 The PROM-project *Polarimetry Influenced by CCN and INP in Cyprus and Chile (PICNICC)* seeks to improve our
269 understanding of aerosol effects on microphysical growth processes in mixed-phase clouds. *PICNICC* exploits unique remote-
270 sensing datasets from the LACROS suite (Radenz et al., 2021) extended with ground-based remote sensing instruments
271 installed at Leipzig University, Universidad de Magallanes (Punta Arenas), and Cyprus University of Technology (Limassol).
272 Thus, dual-frequency polarimetric radar observations from the polluted, aerosol-burden Northern and from the clean, pristine
273 Southern hemisphere can be contrasted for microphysical process studies as already performed in the project for stratiform
274 mixed-phase clouds to investigate inter-hemispheric contrasts in the efficiency of heterogeneous ice formation (Radenz et al.,
275 2021). The PICNICC project challenges the hypothesis that higher ice crystal concentrations favour aggregation, which
276 is expected to be more frequent for high aerosol loads and accordingly higher ice nucleating particle (INP) concentrations,
277 while riming should prevail when supercooled liquid layers are sustained due to a scarcity of INP. Evaluating this hypothesis
278 requires the distinction between aggregation and riming in mixed-phase cloud systems. Fig. 4 demonstrates for a deep mixed-
279 phase cloud system passing the low-aerosol site in Punta Arenas (53°S, 71°W), Chile, on 30 August 2019, the capability of
280 the LACROS suite to distinguish between aggregates and rimed particles when combined with a 94-GHz Doppler radar. The
281 pattern of the 94-GHz radar reflectivity factor (Z , Fig. 4a) underlines the complex structure of the system. The height
282 spectrogram of the vertical-pointing 94-GHz slanted linear depolarization ratio (SLDR, Fig. 4 e) from 08:30 UTC exhibits
283 regions of changing shape signatures and multi-modality in the cloud radar Doppler spectra, where multiple hydrometeor
284 populations coexist. The polarizability ratio ξ_e (Myagkov et al., 2016; Fig. 4d) obtained from the RHI scans of SLDR and the
285 co-cross correlation coefficient of horizontal and vertically polarized channels in the slanted basis ρ , at 35 GHz (Fig. 4 b, c)
286 allows to estimate a density-weighted hydrometeor shape. SLDR is more suited for shape classification compared to LDR. By
287 slanting the polarization basis by 45 deg, the returned LDR signatures are much less sensitive to the canting angle distribution
288 of the targets, especially at low elevation angles (Matrosov et al., 2001; Myagkov et al., 2016). The polarimetric RHI scans
289 and the Doppler spectra data enable the retrieval of the vertical profile of the hydrometeors: Columnar-shaped bullet rosettes
290 are formed between 2.5 km height and cloud top as indicated in the RHI scans by an elevation-constant SLDR (Fig. 4b) and
291 an increase of ρ , with decreasing elevation (Fig. 4c). ξ_e values around 1.3 (Fig. 4d) are characteristic for slightly columnar
292 crystals. The decreasing elevation-dependence of ρ , already at around 3 km height (-15 to -20°C) suggests more random

293 particle orientations; here the W-band SLDR spectra (Fig. 4e) show reduced values, likely due to the co-existence of dendritic
294 ice crystals, which are formed preferably in this temperature range. The co-location of dendrites and columnar crystals can be
295 explained by either splintering of the arms of the dendritic crystals or a mixing of locally produced dendrites with columnar
296 crystals from higher up, or both. Below 2.5 km, ξ_c decreases toward unity, indicating the growth of isometric particles. In
297 addition, the vertical-pointing W-band SLDR slowly decreases toward the cloud base, while fall velocities increase (Fig. 4e).
298 Both features are characteristic for riming, which is corroborated by co-located lidar observations that indicate liquid water in
299 the cloud-base region (not shown). Doppler spectra profiles such as the one presented in Fig. 4e are also used in a new neural-
300 network-based riming detection algorithm recently tailored by Vogl. et al. (2021) for vertical-pointing cloud radar
301 observations. This new approach is insensitive to the mean Doppler velocity, which is - especially at Punta Arenas - strongly
302 influenced by orographic mountain waves, because the radar reflectivity factor, skewness and the edge width of the Doppler
303 spectrum is used instead.

304

305 The PROM-project *Investigating the impact of Land-use and land-cover change on Aerosol-Cloud-precipitation*
306 *interactions using Polarimetric Radar retrievals (ILACPR)* analyzes polarimetric radar observations and model simulations
307 simultaneously in order to improve our understanding of land-aerosol-cloud-precipitation interactions. The Terrestrial Systems
308 Modelling Platform (TSMP; Shrestha et al., 2014; Gasper et al., 2014) developed under the DFG-funded Transregional
309 Research Center TR32 (Simmer et al., 2015) is used to simulate summertime convective storms passing the polarimetric X-
310 band radar (BoXPOL, e.g. Diederich et al., 2015a,b) located in Bonn, Germany. TSMP generally underestimates the convective
311 area fraction, high reflectivities, and the width/magnitude of differential reflectivity (Z_{DR}) columns indicative of updrafts, all
312 leading to an underestimation of the frequency distribution for high precipitation values (Shrestha et al., 2021a). A decadal
313 scale simulation over the region using the hydrological component of TSMP also shows that much of the variability in the
314 simulated seasonal cycle of shallow groundwater could be linked to the distribution of clouds and vegetation (Shrestha, 2021),
315 which further emphasizes the importance of evaluating the representation of clouds and precipitation in numerical models. The
316 fusion of radar observations and models with the aid of observation operators allows for an extended interrogation of the effects
317 of anthropogenic interventions on precipitation generating processes and the capabilities of numerical models to reproduce
318 them. Here, findings from one simulated hailstorm observed on 5 July 2015 passing the city of Bonn, Germany, are explained.
319 Sensitivity simulations are conducted using large-scale aerosol perturbations and different land-cover types reflecting actual,
320 reduced and enhanced human disturbances. While the differences in modelled precipitation in response to the prescribed
321 forcing are below 5 %, the micro- and macrophysical pathways differ, acting as a buffered system to the prescribed forcings
322 (Stevens and Feingold, 2009; Seifert and Beheng, 2012). Fig. 5 shows vertical cross-sections reconstructed from volume scans
323 measured with BoXPOL together with simulated Z_H and Z_{DR} for the TSMP simulations with actual land-cover but perturbed
324 condensation nuclei (CN) and ice nucleating particle (INP) concentrations. CN concentrations are 100 cm^{-3} for maritime and
325 1700 cm^{-3} for continental aerosol. Similarly, default INP concentrations for dust, soot and organics are $162\text{E}3 \text{ m}^3$, $15\text{E}6 \text{ m}^3$
326 and $177\text{E}6 \text{ m}^3$, respectively. For low/high INP, the concentration of soot and organics are decreased/increased by one order of

327 magnitude. To generate the synthetic radar observations the Bonn Polarimetric Radar observation Operator, B-PRO, (Xie et
328 al., 2021; Xie et al., 2016; Heinze et al., 2017; Shrestha et al., 2021b) is applied. B-PRO is based on the non-polarimetric
329 version of EMVORADO (Zeng et al., 2016); its code part for computing unattenuated radar reflectivity on the original model
330 grid (Blahak, 2016) has been expanded to unattenuated polarimetric variables based on spheroidal shape assumptions (T-
331 matrix). Because the full polarimetric version of EMVORADO (Pol-EMVORADO, see Section 4.1) was only released very
332 recently, the model data in ILACPR has been processed using B-PRO. Preliminary comparisons between B-PRO and Pol-
333 EMVORADO (not shown here) exhibit negligible differences in their results on the model grid, but Pol-EMVORADO is much
334 more computationally efficient and takes effects of beam broadening and attenuation along the actual radar ray paths into
335 account. The vertical cross sections are compared at different times marked by the vertical grey bars in the time series of
336 Convective Area Fraction (CAF, Fig. 5 a), defined as the ratio of area with $Z_H > 40$ dBZ (at 2 km a.g.l.) to total storm area. On
337 average BoXPol observations show a bit higher CAF compared to the simulations. The evolution is always similar in terms of
338 an initial increase and intensification in the second part of the observation period, where the experiment with maritime aerosols
339 and low INP (Mar-lowIn) is closest to the observations. All simulations show Z_H and Z_{DR} patterns comparable to BoXPol
340 observations, however, the experiment with continental aerosol and default INP (Con-defIN, Fig. 5c) shows weaker Z_H while
341 Mar-lowIN (Fig. 5d) shows somewhat higher Z_H values compared to BoXPol (see Fig 5a). The simulations with maritime CN
342 produce low cloud droplet concentrations with larger mean diameters compared to the simulations with continental CN.
343 Accompanied by a very strong updraft, this also leads to high concentrations of supercooled raindrops above the melting layer
344 with broader spatial extent (due to a broader updraft region) compared to the simulations with continental CN and contributes
345 to an enhanced growth of hail resulting in higher Z_H . Also, as shown in the CAF time series, simulations with continental
346 aerosol and default/high IN tend to exhibit similar behaviour in radar space, with the latter exhibiting higher CAF only at latter
347 stages of the storm. The continental CN simulations with default and high IN differ in terms of simulated updraft speed and
348 total hydrometeor content, being higher for the latter one. However, Cont-highIN produces smaller graupel and hail particles
349 compared to Cont-defIN, resulting in similar Z_H . The experiment with continental aerosol and high INP concentration (Con-
350 highIN, not shown) generates similar polarimetric moments to Con-lowIN. All experiments exhibit vertically extensive
351 columns of (slightly) enhanced Z_{DR} , collocated with intense simulated updrafts reaching up to 13 to 14 km. Indeed, Z_{DR}
352 columns emerged as proxies for updraft strength and ensuing precipitation enhancement (Weissmann et al., 2014; Simmer et
353 al., 2014; Kumjian et al., 2014; Kuster et al., 2020), and research on their exploitation for nowcasting and data assimilation is
354 ongoing. In Fig. 5c/d synthetic Z_{DR} columns are vertically extensive, while Z_{DR} values within the column stay below 0.3 dB.
355 BoXPol observations show Z_{DR} columns reaching up to 6 km height only but with Z_{DR} values exceeding 1dB. While Z_{DR} values
356 in the lower part of the columns are mostly generated by large raindrops, freezing drops and wet hail determine Z_{DR} in the
357 upper parts of the column (Kumjian et al., 2014; Snyder et al., 2015). The diverging appearance of observed and synthetic Z_{DR}
358 columns may point to deficiencies in the treatment of raindrops undergoing freezing and motivates further research. Too rapid
359 freezing of drops combined with graupel generated from the frozen drops may generate enhanced but still low Z_{DR} up to high
360 altitudes. Following Ilotoviz et al. (2018) such attributes of Z_{DR} columns are highly determined by the vertical velocity, hail

361 size, and aerosol concentration, e.g. higher CN concentrations lead to higher columns with higher Z_{DR} values inside and also
362 higher Z_H . In this case study and the specific time step shown, Mar-lowIN (i.e. with lower CN concentration) shows a wider
363 and somewhat taller Z_{DR} column together with a more intense Z_H core (compare Fig. 5c/d). Further explanations require an
364 improved representation of the Z_{DR} columns in the model.

365 **4 Fusion of radar polarimetry and atmospheric models**

366 Probably the most important and central tool for connecting polarimetric observations with numerical atmospheric models are
367 observation operators, which generate virtual observations from the model state. These virtual observations can be
368 directly compared with the real observations and signatures of microphysical processes including their temporal evolution.
369 Thus, the accuracy of precipitation and cloud parameterizations can be indirectly evaluated and a database established for
370 model optimization. Missing polarimetric process fingerprints (e.g. Kumjian, 2012) in the virtual observations may hint at
371 model deficiencies, and model parameterizations can be adapted in order to increase the coherence between real and virtual
372 observations. Moreover, sufficiently accurate and fast observation operators are mandatory for the direct assimilation of
373 observations using ensemble methods.

374 However, bulk cloud microphysical parameterizations required for NWP models include assumptions on several critical
375 parameters and processes which are not explicitly prognosed or resolved by the governing numerical model. An example are
376 the inherently assumed particle size distributions and their relations to the prognostic moments (hydrometeor mass and number
377 densities). Another challenge is the handling of hydrometeor parameters that are not or only insufficiently constrained by the
378 model's microphysics but are highly relevant for the calculation of virtual observations in the (radar) observation operator. For
379 example, the melting state as well as shape, microstructure, and spatial orientation of the different hydrometeors are not
380 prognostic (or not even implicitly assumed) in most operational bulk schemes. Therefore, suitable assumptions are required in
381 observation operators in order to compute meaningful virtual observations. Moreover, bulk cloud microphysical schemes may
382 only insufficiently approximate the natural variability, and the interactions between the few assumed hydrometeor classes and
383 the size distribution moments are mainly tuned to get, e.g., the surface precipitation right. The current approximations in both
384 numerical models and observation operators may hence translate into different sources of errors and biases of the simulated
385 radar variables (e.g. Schinagl et al., 2019; Shrestha et al., 2021b). As an example, Fig. 7 shows too low polarimetric signals
386 above the melting layer, which are partly caused by assumptions inherent in the observation operator (see Sect. 4.2.1). Such
387 problems challenge both model evaluation and data assimilation. Accordingly, central science questions concern the realism
388 of the sensitivities of simulated radar variables to parameters in the observation operators and the models as well as effective
389 approaches for the evaluation and improvement of moist processes parameterizations.

390 Another challenge for large-scale applications such as long-term model evaluations or operational real-time data assimilation
391 based on large radar networks is the high computational demand and low speed of current polarimetric radar observation
392 operators. Often, the operators apply some kind of pre-calculated lookup tables (LUT) of scattering properties and

393 parallelization techniques for speed optimizations (e.g. Wolfensberger and Berne, 2018; Matsui et al., 2019; Oue et al., 2020).
394 Despite that, radar simulations for a single time step take - depending on the computer - on the order of minutes for one single
395 plan position indicator (PPI) scan (Wolfensberger and Berne, 2018) or for a single model scene (CR-SIM; Oue et al., 2020).
396 Matsui et al. (2019) state the LUT generation process of their POLARRIS operator to only take a few minutes when distributed
397 to few thousands of processors, but do not elaborate on the required times for the actual simulation of the radar measurement.
398 The operator B-PRO (Xie et al., 2016), which uses neither of these techniques, is much slower, as applications within SPP-
399 PROM have demonstrated (Shresta et al., 2021b). While acceptable for research, real-time operational applications may pose
400 much stricter time constraints. Therefore, an important technical goal is to provide an efficient, yet physically accurate and
401 “state-of-the-art”, polarimetric radar operator to the community, which reduces the simulation time for multi-elevation PPI
402 scans of many stations to a few seconds.

403 **4.1 Polarimetric radar observation operator development**

404 Within the PROM-project *Operation Hydrometeors*, the up-to-now non-polarimetric radar observation operator
405 EMVORADO (Zeng et al., 2016; Blahak and de Lozar, 2020; Blahak, 2016) has been extended to polarimetry (Mendrok et
406 al., 2021). (Non-polarimetric) EMVORADO has been designed to efficiently simulate PPI volume scan measurements of entire
407 radar networks from the prognostic model state of an NWP model for direct comparisons with the radar observations.
408 EMVORADO is part of the executable of both the COSMO and ICON NWP models, which allows to run the operator within
409 a NWP model run and to access the model state and radar variables in memory. The code is MPI- and OpenMP-parallelized
410 and thus fully exploits the computational power of modern HPCs and avoids storing and re-reading extensive model state data
411 to/from hard drives. This enables large-scale real-time applications such as operational data assimilation and extensive NWP
412 model verifications using whole radar networks at high temporal resolution. Its modular nature allows for relatively easy
413 interface development to other NWP models. An offline framework is also available, which accesses model states of one model
414 time step from hard disk. EMVORADO includes detailed modular schemes to simulate beam bending, beam broadening and
415 melting effects, and allows users to choose for each process between computationally cheap and physically accurate options.
416 The operator has been used for the assimilation of radar reflectivity with positive impact on precipitation forecasts (Bick et al.,
417 2016; Zeng et al., 2018; 2019; 2020). Currently, DWD uses EMVORADO to operationally assimilate 3D volumetric
418 reflectivity and radial wind observations of its C-band radar network. Key for this application is also the extensive use of
419 precomputed lookup tables that relate (Mie-theory based) bulk reflectivity directly to hydrometeor densities and temperature.
420 The effects of neglecting radar beam pattern and broadening and of hydrometeor fall speeds on data assimilation have been
421 investigated in a joint effort together with the PROM-project *Representing model error and observation Error uncertainty
422 for Data assimilation of POLarimetric radar measurements (REDPOL)* (Zeng et al., 2021a).
423 The polarimetry-extended EMVORADO, in the following referred to as Pol-EMVORADO, has inherited all features of
424 EMVORADO, which in turn have been expanded where necessary to calculate and handle polarimetric variables. This
425 includes, e.g., beam bending, beam broadening, and beam smoothing schemes, effective medium approximations allowing 1-

426 and 2-layered hydrometeors with different water-ice-air mixing schemes and melting topologies, and a lookup table approach
427 for an efficient access to polarimetric observables such as Z_{DR} , LDR , ρ_{HV} , and K_{DP} . Optionally, attenuation effects can be
428 considered, specific and differential attenuation (A_H and A_{DP} , respectively) provided, and further output quantities derivable
429 from the complex scattering amplitudes easily added. Pol-EMVORADO applies state-of-the-art scattering properties of
430 spheroidal particles derived by one-layered (Mishchenko, 2000) and two-layered T-Matrix approaches (Ryzhkov et al., 2011).
431 Assumptions on spheroid shape and orientation follow parameterizations introduced in Ryzhkov et al. (2011). The lookup
432 table approach has been revised to accommodate additional parameters necessary to derive the full set of polarimetric radar
433 output. For a given set of parameters affecting the hydrometeor scattering properties, the lookup tables are created only once,
434 stored in files, and re-used for subsequent runs.

435 Using pre-existing lookup tables, the computations for virtual polarimetric volume scans of radar networks are very fast.
436 Foreexample, simulating the volume scan observations of all polarimetric parameters for all 17 German radars takes a few
437 seconds only on a Linux workstation (8 cores) and adds only about 1 s per radar output time step to the model runtime when
438 performed online during a run of ICON-D2 (DWD's operational convection-allowing ICON version with 2 km grid spacing)
439 on DWD's NEC Aurora supercomputer. That is, simulating polarimetric radar data in intervals of 5 min as observed by DWD's
440 weather radar network adds only a few percent of the total model runtime (Mendrok et al., 2021) enabling the exploitation of
441 Pol-EMVORADO for the assimilation of high temporal resolution polarimetric radar data in an operational framework. Pol-
442 EMVORADO has been incorporated into the official version of EMVORADO and can be run online (i.e. within a COSMO
443 or ICON run) as well as offline (i.e. stand-alone with model fields from data files). Although designed as a PPI volume scan
444 observation operator for a radar network, its output can also be provided on NWP model grids. An example of a Z_{DR} volume
445 scan simulated by Pol-EMVORADO for the **REDPOL** project is shown in Fig. 6 (see also Sect. 4.2.3).

446 In summary, (Pol-)EMVORADO comprises a wide set of state-of-the-art features. While each of these features is provided
447 also by other observation operators, (Pol-)EMVORADO is, to our knowledge, unique in combining them into one operator
448 that allows to simulate virtual observations, including instrumental effects and in formats directly comparable to real
449 observational scans, from NWP model runs in a comparably accurate and very fast manner targeted at operational applications.
450 Mendrok et al. (2021) give a comprehensive description of the features developed or updated for Pol-EMVORADO including
451 details on their implementation and performance.

452 However, from the application of Pol-EMVORADO (or B-PRO, see Sect. 3.2) within PROM, a number of problems became
453 evident. Modeling hydrometeors as homogeneous effective-medium particles (e.g. oblate spheroids) does not reproduce well
454 the polarimetric signatures of low density hydrometeors like dendrites or aggregates typical for snow while keeping their
455 microphysical properties (e.g. aspect ratio, degree of orientation) within realistic - observed or model-predicted - ranges and
456 consistent between different radar frequencies. This deficiency has been demonstrated and explained from electromagnetic
457 theory by Schrom et al. (2018). It is obvious in one case study (Shrestha et al., 2021b) and in Fig. 7, where Z_{DR} and K_{DP} in the
458 snow-dominated layer between 2.5 and 5 km height almost entirely lack the typical observed features, i.e. bands of enhanced
459 Z_{DR} and K_{DP} in the dendritic growth layer that then smoothly decrease to mostly positive, non-zero values towards the melting

460 layer. This deficiency can also be observed with other polarimetric observation operators applying a T-matrix approach (see
461 simulation-to-observation comparisons in Wolfensberger and Berne (2018), Matsui et al. (2019), Oue et al. (2020), where the
462 lack of Z_{DR} and K_{DP} signatures is not discussed at all or exclusively explained by a lack of secondary ice, though), which
463 nevertheless currently constitutes the state-of-the-art in radar polarimetry. Orientation and shape of frozen and melting
464 hydrometeors are very variable, both in nature and in the assumptions used in observation operators, which translates into large
465 uncertainties in polarimetric radar signatures (e.g., Matsui et al., 2019; Shrestha et al., 2021b).

466 To tackle these challenges, it is planned to interface Pol-EMVORADO to scattering databases or other scattering models in
467 order to enable more realistic cloud ice and aggregate snowflake scattering properties and allow for improvements or
468 extensions of the polarimetry-related microphysical assumptions (shape/habit/microstructure, orientation and their
469 distribution, e.g., Wolfensberger et al., 2018), particularly for (partly-)frozen hydrometeors. For PROM's 2nd phase, we have
470 proposed to take this up guided with Lagrangian particle model information as well as to test the application of Pol-
471 EMVORADO in an operational data assimilation environment.

472 **4.2 Model evaluation and improvements using forward simulations and microphysical retrievals**

473 **4.2.1 Convection-resolving simulations with COSMO**

474 In a joint effort, the PROM-projects *Operation Hydrometeors* and *ILACPR* evaluate simulated stratiform precipitation events
475 in radar observation space and develop a sophisticated polarimetry-based hydrometeor classification and quantification for the
476 evaluation of the representation of hydrometeors in numerical models. Based on a stratiform event monitored on 7 October
477 2014 with the Bonn polarimetric X-band radar BoXPoL, Fig. 7 illustrates the potential of using polarimetric observations for
478 the evaluation and improvement of microphysical parameterizations. Fig. 7 a-f compare QVPs of measured and virtual Z_H ,
479 Z_{DR} , and K_{DP} with the Bonn Polarimetric Radar observation Operator B-PRO (Xie et al., 2021) to forecasts simulated with
480 COSMO version 5.1 using its 2-moment cloud microphysics scheme (itype_gscp=2683; Seifert and Beheng, 2016). Due to a
481 small spatial shift of the precipitation event in the simulations, the observations at 50.7305 N, 7.0717 E are compared with
482 simulations at a close-by grid point at 51.1 N, 7.0717 E. As demonstrated in Shrestha et al. (2021b) using a similar stratiform
483 precipitation event, COSMO tends to simulate considerable amounts of melting graupel partly reaching the surface, which
484 results in higher synthetic Z_{DR} than observed (compare Fig. 7c/d) within and below the melting layer (ML). Above the ML,
485 however, synthetic Z_{DR} already approaches 0 dB at around 6 km height, which indicates deficiencies in the ice-snow
486 partitioning in COSMO as well as in the assumed snow morphology (soft spheroids) in the observation operator, both resulting
487 in too low polarimetric signals. While the observed and simulated Z_H is comparable in terms of structure and magnitude -
488 except a more pronounced observed ML - larger differences exist with respect to K_{DP} above the ML (Fig. 7e/f). While
489 observations show bands of enhanced K_{DP} within the dendritic growth layer (DGL) centred around -15°C , the simulated K_{DP}
490 is very weak indicating a lower concentration of crystals and early aggregates compared to observations (e.g. Moisseev et al.,
491 2015). Ice water content (IWC) above the ML retrieved from measured K_{DP} and differential reflectivity in linear scale Z_{dr} , i.e.
492 $IWC(K_{DP}, Z_{dr})$ following Ryzhkov et al. (2018), agrees well with IWC modelled by COSMO in terms of structure, but has

493 lower magnitudes (compare Fig. 7 g/h) in line with the lower simulated K_{DP} . Overall, Fig. 7 supports the hypothesis of a too
494 strong graupel production in the simulations. *Operation Hydrometeors* also developed a robust radar-based hydrometeor
495 classification (HMC) and mixing ratio quantification algorithm following Grazioli et al. (2015) and Besic et al. (2016, 2018)
496 for the evaluation of the representation of hydrometeors in NWP models (standard output is the dominant hydrometeor type
497 only). This HMC is based on clustering and has the advantage that the radar data are separated into clusters based on their
498 polarimetric similarity (no theoretical preliminary calculation is needed), which are then identified as hydrometeor classes.
499 Various clustering methods can be used here (e.g. Lukach et al. (2021)). The new method is relatively insensitive to
500 uncertainties in the scattering properties of ice particles. Its application to the BoXPoI observations does not indicate graupel
501 below the ML (Fig. 8a), while COSMO simulates a pronounced, thick graupel layer (Fig. 8b) including some melting graupel
502 particles reaching the ground around at 1:45 UTC. Applying the HMC to the virtual observations, however, does not reproduce
503 a graupel layer of similar intensity (Fig. 8c), probably caused by a too strong Z_H and temperature influence (compare with Fig.
504 7) relative to the polarimetric variables in the classification scheme which needs further investigation. A persistent challenge
505 in according routines is that clusters are always separated by the 0 °C-level (e.g. Ribaud et al., 2019), i.e. hail or graupel are
506 identified as clusters only below or above the melting layer. For the case study in Shrestha et al. (2021b) the simulated graupel
507 layer was even more pronounced and sensitivity experiments were performed to guide model improvement: increasing the
508 minimum critical particle diameter D_{crit} , which is required for self-collection of ice particles (aggregation) increased/improved
509 the ice-snow partitioning, and a lower temperature threshold for snow and ice riming, T_{rime} , considerably reduced the graupel
510 production.

511 Comparing state-of-the-art polarimetric retrievals of liquid water content (LWC), ice water content (IWC), particle number
512 concentration N_t and mean particle diameter D_m (e.g. Ryzhkov et al., 2018; Ryzhkov and Zrnica, 2019; Bukovčić et al., 2020;
513 Reimann et al., 2021; Trömel et al., 2019) with their simulated counterparts can also be used for evaluating NWP models and
514 for data assimilation (Carlin et al., 2016). Fig. 7g/h, e.g., shows higher $IWC(K_{DP}, Z_{dr})$ than simulated by COSMO for the case
515 study discussed earlier. However, for more solid conclusions about possible model errors, as well as for the use of retrieved
516 quantities for data assimilation, the retrieval uncertainties must be estimated. The analysis of data collected in the ice regions
517 of tropical convective clouds indicates e.g., that $IWC(K_{DP}, Z_{dr})$ yields a root-mean-square error of 0.49 gm^{-3} with the bias
518 within 6% (Nguyen et al., 2017; 2019). Murphy et al. (2020) introduced the columnar vertical profile (CVP) methodology to
519 follow the track of research aircrafts and better co-locate in-situ data to radar microphysical retrievals. Applying the
520 methodology to two mesoscale convective systems, they found the best performance of polarimetric microphysical retrievals
521 in regions of high Z_{DR} and high K_{DP} but recommend a much larger dataset to finally conclude on the accuracy of these retrievals.

522
523 The PROM-project *POLarimetric signatures of ICE microphysical processes and their interpretation using in-situ*
524 *observations and cloud modelling (POLICE)* evaluates radar retrievals and models using in particular in-situ observations of
525 microphysical cloud parameters from the research aircrafts HALO (e.g. Wendisch et al., 2016; Voigt et al., 2017) and Falcon
526 (e.g. Voigt et al., 2010; Voigt et al., 2014; Flamant et al., 2017). Currently, ground-based polarimetric radar measurements and

527 aircraft in-situ data from the Olympic Mountain Experiment OLYMPEX (Houze et al., 2017; Heymsfield et al., 2018) are
528 exploited to investigate riming processes and to evaluate retrievals of ice water content (IWC), particle number concentration
529 N_t , and mean particle diameter D_m (e.g. Ryzhkov et al., 2018; Ryzhkov and Zrnica, 2019; Bukovčić et al., 2020; Carlin et al.
530 2021). The OLYMPEX mission took place on the Olympic Peninsula of Washington State (USA) from November 2015
531 through February 2016. University of North Dakota's (UND) Cessna Citation II equipped with an in-situ cloud payload
532 overpassed the National Science Foundation (NSF) Doppler On Wheels (DOW, mobile polarimetric X-band radar with about
533 60 km range and 74 m radial resolution), placed in the Chehalis Valley at Lake Quinault (47.48 N, 123.86 W, 64 m altitude)
534 performing RHI scans within an azimuthal sector of 22 deg. Measurements and microphysical retrievals of the DOW and the
535 Citation, respectively, are currently evaluated and will then be compared at matched space-time coordinates for several flight
536 transects.

537

538 **4.2.2 Climate simulations with ICON-GCM**

539 A major part of the uncertainties in representing clouds and precipitation in atmospheric models can be attributed to unresolved
540 variability that affects resolved variables via non-linear processes. Current climate model horizontal resolutions are on the order
541 of 100 km. But even for NWP models, which have resolutions between 10 km for global and 1 km for regional simulations,
542 most cloud processes remain unresolved. The project *Climate model Parameterizations informed by Radar (PARA)*
543 evaluates and improves the representation of cloud and precipitation processes in particular for climate models and focuses on
544 precipitation formation in ice clouds. Since most surface precipitation over continents and extra-tropical oceans involve the
545 ice phase (Mülmenstädt et al., 2015; Field and Heymsfield, 2015) its reliable representation is paramount and thus the focus
546 of *PARA*. Microphysical parameterizations typically consider only the mean cloud liquid or ice water content to compute
547 process rates, which causes biases in all nonlinear processes including radiation (e.g., Cahalan, 1994; Carlin et al., 2002) and
548 precipitation formation (e.g., Pincus and Klein, 2000). Realistic results thus require the tuning of process rates (e.g., Rotstayn,
549 2000) or realistic estimates of subgrid-scale cloud variability and its inclusion in the process parameterizations. To tackle this
550 issue, *PARA* exploits inherent model assumptions for treating fractional cloudiness. Since the early works of Sommeria and
551 Deardorff (1977), atmospheric models assume or predict some notion of subgrid-scale variability of relative humidity. Some
552 models do so by predicting cloud fraction (e.g., Tiedtke, 1993), others use a diagnostic representation of the subgrid-scale
553 probability density function (PDF) of total water specific humidity, q_t (e.g., Sundqvist et al., 1989; Smith, 1990; Le Treut and
554 Li, 1991; Rosch et al., 2015). Another option is to utilize a prognostic probability density function (PDF) of q_t by assuming a
555 functional form and predicting the shape parameters of the PDF (e.g., Tompkins, 2002; Neggers, 2009). The German climate
556 and weather prediction model ICON in its version dedicated to climate simulations (general circulation model version; ICON-

557 GCM) inherits the representation of physical processes from its predecessor ECHAM6 (Stevens et al., 2013) and uses the
558 Sundqvist et al. (1989) parameterization for a diagnostic PDF of the total-water specific humidity, q_t .

559 As a first step, *PARA* analyses the implied PDF of cloud ice using satellite observations from combined CloudSat-CALIPSO
560 radar-lidar satellite observations (DARDAR, Delanoë et al., 2014). Interestingly, a first direct comparison of IWC profiles
561 obtained from DARDAR with polarimetric retrievals based on the ground-based BoXPol radar shows an overall good
562 agreement, except for columns with an integrated ice water path $IWP > 1 \text{ kg m}^{-2}$. In these regions pronounced polarimetric
563 signatures result in high IWC at higher altitudes, which are neither reproduced by reflectivity-only retrievals nor by the
564 DARDAR retrievals. The statistics are currently evaluated on a larger database, which is also used to investigate the impact
565 on the parameterizations in ICON-GCM. In the second step, a stochastic parameterization approach is taken to allow for an
566 unbiased computation of cloud microphysical process rates on average. Based on the cumulative distribution function (CDF),
567 a random number generator draws from the CDF according to the simulated likelihood a plausible value of the specific ice
568 mass based on which the microphysical process is computed. This specifically considers the formation of solid precipitation
569 (snow) from ice clouds via aggregation and accretion processes (Lohmann and Roeckner, 1996; Stevens et al., 2013), and
570 subsequently the evaporation of precipitation below the clouds. The result of the revised aggregation parameterization is shown
571 in Fig. 9. The increased aggregation rate, which is a linear function of the specific cloud ice, q_i , leads to an average decrease
572 in q_i . The aggregation rate is directly linked to the accretion rate, which lowers the effect of q_i decrease. An investigation of
573 the influence of the revised aggregation parameterization on the different microphysical process rates - which are related to
574 the ice phase - is currently performed. A detailed evaluation of the new versus old parameterization with the ground-based
575 polarimetric radar is on its way, and will in particular focus on the time scales of evaporation of precipitation below the cloud.

576 **4.2.3 Data assimilation**

577 Within an idealized framework, Jung et al. (2008; 2010) and Zhu et al. (2020) demonstrated benefits of assimilating simulated
578 polarimetric data for the estimation of microphysical state variables. Up to now, however, direct assimilation of real
579 polarimetric data poses great challenges due to the deficiencies of cloud and precipitation schemes in NWP models in
580 realistically representing and providing the necessary information (optimally the distribution of particle size, shape and
581 orientations in all model grid boxes) required by a polarimetric radar observation operator and therefore causing large
582 representation error (Janjic et al., 2018). Both the specification of model error to examine uncertainty in microphysics (Feng
583 et al., 2021) and the specification of the observation error for polarimetric radar observations that include estimates of the
584 representation error (Zeng et al., 2021b), are investigated in the PROM-project *REDPOL*. For the assimilation of radar
585 reflectivity with an ensemble Kalman filter, several approaches for including model errors during data assimilation are
586 explored, including 1) additive noise with samples representing large-scale uncertainty (see Zeng et al., 2018), 2)
587 combination of large scale and unresolved scale uncertainty (Zeng et al., 2019), and finally 3) adding to these warm bubble
588 triggering of convective storms in case they are missing in the one hour forecast but present in corresponding observations

589 (Zeng et al., 2020). Applying Pol-EMVORADO to the analysis obtained by assimilating radar reflectivity from the German
590 C-band network), Fig. 6 illustrates the resulting differences of these three techniques in Z_{DR} -space. Obviously, synthetic Z_{DR}
591 values depend on the strategy used to specify the model error, putting another weight to the argument that assimilation of radar
592 reflectivity alone is not sufficient to constrain the estimation of microphysical state variables, and that polarimetric information
593 is required in addition. First results in this direction were reported by Putnam et al. (2019), who assimilated Z_{DR} below the
594 melting layer but reported problems with the assimilation of K_{DP} data for a supercell case due to high observation errors as a
595 result of contamination from wet hail, dust and debris and nonuniform beam filling.

596 .

597 **5 Summary and Perspectives**

598 The Priority Programme *Polarimetric Radar Observations meet Atmospheric Modelling (PROM)* (SPP 2115,
599 <https://www2.meteo.uni-bonn.de/spp2115/>) was established in April 2017 by the Senate of the Deutsche
600 Forschungsgemeinschaft (DFG, German Research Foundation) and is designed to run for six years. PROM is a coordinated
601 effort to foster partnerships between cloud modelers and radar meteorologists and thus to accelerate the exploitation of
602 polarimetric weather radars to improve the representation of cloud and precipitation processes in numerical models. The first
603 funding phase engaged in an as-complete-as-possible exploitation and understanding of nation-wide polarimetric
604 measurements complemented by state-of-the-art measurement devices and techniques available at supersites. Bulk
605 polarimetric measurements available over Germany are complemented with multi-frequency observations and spectral
606 polarimetry for detailed studies of ice and cloud microphysics. Thus, modellers now hold an unprecedented amount of three-
607 dimensional microphysics-related observational data in their hands to improve parameterizations. Key tools for the fusion of
608 radar polarimetry and atmospheric modelling, e.g. the Monte-Carlo Lagrangian particle model McSnow and the polarimetric
609 observation operator Pol-EMVORADO, have been developed. PROM started with detailed investigations of the representation
610 of cloud and precipitation processes in the COSMO and ICON atmospheric models exploiting polarimetric observation
611 operators. First improvements of the 2-moment cloud- and precipitation microphysics scheme are made and more are expected
612 in phase 2. In addition, intercomparisons of microphysics schemes in radar space have been performed. Phase 1 further
613 developed microphysical retrievals, determined their uncertainties and started their exploitation for model evaluation and
614 radar-informed parameterizations. The developed prerequisites pave the way to finally exploit polarimetry for indirect and
615 direct data assimilation in the upcoming second funding phase.

616 Some tools developed in phase 1, however, still require refinement in phase 2. The T-matrix calculations for
617 electromagnetic scattering by spheroidal particles represent only a crude approximation to frozen and mixed-phase
618 hydrometeors, especially for pristine ice particles and aggregate snowflakes at cloud radar wavelengths. It is not possible to
619 reproduce observed polarimetric signatures of snow with the T-Matrix approach (i.e. homogeneous ice-air spheroids) and

620 realistic microphysics (shape, orientation). Refinements include interfacing to a new discrete dipole approximation (DDA)-
621 based scattering data base for realistic ice and snow particles for all relevant weather radar wavelengths and improvements of
622 the melting scheme of graupel and hail.

623 Based on the progress made, the fusion of radar polarimetry and atmospheric modelling can be approached even more
624 aggressively in phase 2. While objective 1 received most attention in phase 1, more projects will exploit the observational
625 insights and tools developed to finally improve parameterizations and assimilate polarimetric information, i.e. more emphasis
626 will be put on objectives 2 and 4 in phase 2. Direct assimilation of polarimetric variables remains challenging, because NWP
627 models need to realistically represent and provide the necessary information required by a polarimetric radar observation
628 operator; ideally the distribution of particle size, shape and orientation would be required in all model grid boxes. Indirect
629 assimilation of polarimetric information (e.g. microphysical retrievals, and process signatures), however, is less demanding to
630 the model and should be pursued in parallel. Modern Bayesian data assimilation techniques are sensitive to both model- and
631 observation operator biases, so that further work on these issues is of great importance for a successful data assimilation.

632

633 **Data availability**

634 The data presented in this paper are available through the authors upon request. Polarimetric radar data from the operational
635 C-band radar network is also available from the German Weather Service (DWD). Specific campaign data will be published
636 in addition.

637

638 **Author contributions**

639 Silke Trömel had the initial idea and mainly organized and structured the joint publication. Silke Trömel, Johannes Quaas, and
640 Clemens Simmer formed the editorial team consolidating the text. All authors contributed to specific sections of the paper and
641 commented on the paper.

642

643 **Competing interests**

644 Johannes Quaas is editor of ACP. The authors declare to have no additional conflict of interest.

645

646 **Special issue statement**

647 This article is the overview article of the ACP/AMT/GMD inter-journal special issue “Fusion of radar polarimetry and
648 numerical atmospheric modelling towards an improved understanding of cloud and precipitation processes”. It is not associated
649 with a conference.

650

651 **Acknowledgments**

652 We gratefully acknowledge the funding of the German Research Foundation (DFG) to initialize the special priority program
653 on the Fusion of Radar Polarimetry and Atmospheric Modelling (SPP-2115, PROM). The work of contributing authors was
654 carried out in the framework of the projects Operation Hydrometeors (Grants TR 1023/16-1 and BL 945/2-1), IcePolCKa (HA
655 3314/9-1 and ZI 1132/5-1), ILACPR (Grant SH 1326/1-1), IMPRINT (Grant KN 1112/3-1), POLICE (Grants TR 1023/13-1
656 and VO 1504/5-1), PARA (Grants QU 311/21-1 and TR 1023/15-1), HydroColumn (Grant FR 4119/1-1), REDPOL (Grant JA
657 1077/5-1), and PICNICC (Grants KA 4162/2-1 and SE 2464/1-1). ILACPR gratefully acknowledges the computing time
658 (project HBN33) granted by the John von Neumann Institute for Computing (NIC)
659 and provided on the supercomputer JUWELS at Jülich Supercomputing Centre (JSC).

660

661

662 **References**

663 Alfieria, L., Thielen, J., and Pappenberger, J.: Ensemble hydro-meteorological simulation for flash flood early detection in
664 southern Switzerland, *J. Hydrol.*, 424, 143-153, doi:10.1016/j.jhydrol.2011.12.038, 2012.

665 Bauer, P., Thorpe, A., and Brunet, G.: The quiet revolution of numerical weather prediction, *Nature* 525, 47–55,
666 doi:10.1038/nature14956, 2015.

667 Besic, N., Gehring, J., Praz, C., Figueras i Ventura, J., Grazioli, J., Gabella, M., Germann, U., and Berne, A.: Unraveling
668 hydrometeor mixtures in polarimetric radar measurements, *Atmos. Meas. Tech.*, 11, 4847–4866, doi:10.5194/amt-11-4847-
669 2018, 2018.

670 Besic, N., Figueras i Ventura, J., Grazioli, J., Gabella, M., Germann, U., and Berne, A.: Hydrometeor classification through
671 statistical clustering of polarimetric radar measurements: A semisupervised approach. *Atmos. Meas. Tech.*, 9(9), 4425-4445,
672 2016

673

674 Bick, T., Simmer, C., Trömel, S., Wapler, K., Stephan, K., Blahak, U., Zeng, Y., and Potthast, R.: Assimilation of 3D-radar
675 Reflectivities with an Ensemble Kalman Filter on the Convective Scale, *Quart. J. Roy. Meteor. Soc.*, 142, 1490–1504, 2016.

676

677 Blahak, U.: RADAR_MIE_LM and RADAR_MIELIB - Calculation of Radar Reflectivity from Model Output, COSMO
678 Technical Report No. 28, Consortium for Small Scale Modeling (COSMO), available online [http://www.cosmo-
679 model.org/content/model/documentation/techReports/docs/techReport28.pdf](http://www.cosmo-model.org/content/model/documentation/techReports/docs/techReport28.pdf), 2016.

680

681 Blahak, U. and De Lozar, A.: EMVORADO - Efficient Modular VOLUME scan RADAR Operator. A User's Guide, Deutscher
682 Wetterdienst, available online http://www.cosmo-model.org/content/model/documentation/core/emvorado_userguide.pdf,
683 2020.

684

685 Brdar, S. and Seifert, A.: McSnow: A Monte-Carlo Particle Model for Riming and Aggregation of Ice Particles in a
686 Multidimensional Microphysical Phase Space, *J. Adv. Model. Earth Syst.*, 10(1), 187–206, doi:10.1002/2017MS001167, 2018.

687

688

689 Bukovčić, P., Ryzhkov, A., and Zrnić, D.: Polarimetric Relations for Snow Estimation—Radar Verification, *Journal of Applied
690 Meteorology and Climatology*, 59(5), 991-1009, doi:10.1175/JAMC-D-19-0140.1, 2020

691

692 Bühl, J., Seifert, P., Wandinger, U., Baars, H., Kanitz, T., Schmidt, J., Myagkov, A., Engelmann, R., Skupin, A., Heese, B.,
693 Klepel, A., Althausen, D., and Ansmann, A.: LACROS: The Leipzig Aerosol and Cloud Remote Observations System, in:
694 *SPIE Remote Sensing*, edited by Comeron, A., Kassianov, E. I., Schäfer, K., Stein, K., and Gonglewski, J. D., p. 889002,
695 Dresden, Germany, doi:10.1117/12.2030911, 2013.

696

697 Bühl, J., Seifert, P., Maygkov, A., and Ansmann, A.: Measuring ice- and liquid-water properties in mixed-phase cloud layers
698 at the Leipzig Cloudnet station, *Atmos. Chem. Phys.*, 16, 10609-10620, doi: 10.5194/acp-16-10609-2016, 2016

699

700 Cahalan, R. F.: Bounded cascade clouds: albedo and effective thickness, *Nonlinear Proc. In Geophysics.*, 1, 156-167, 1994.

701

702 Carlin, B., et al.: High-cloud horizontal inhomogeneity and solar albedo bias, *J. Climate*, 15, 2321 – 2339, 2002.

703

704 Carlin, J. T., Ryzhkov, A. V., Snyder, J. C., and Khain, A.: Hydrometeor Mixing Ratio Retrievals for Storm-Scale Radar Data
705 Assimilation: Utility of Current Relations and Potential Benefits of Polarimetry, *Mon. Weather Rev.* 144(8), 2981-3001,
706 doi:10.1175/MWR-D-15-461 0423.1., 2016.

707

708 Carlin, J. T., Reeves, H. D., and Ryzhkov, A. V.: Polarimetric Observations and Simulations of Sublimating Snow:
709 Implications for Nowcasting. *J. Appl. Meteor. Climatol.*, 60(8), 1035-1054, doi:10.1175/JAMC-D-21-0038.1, 2021.

710

711 Costa-Surós, M., Sourdeval, O., Acquistapace, C., Baars, H., Carbajal Henken, C., Genz, C., Hesemann, J., Jimenez, C., König,
712 M., Kretschmar, J., Madenach, N., Meyer, C. I., Schrödner, R., Seifert, P., Senf, F., Brueck, M., Cioni, G., Engels, J. F., Fieg,
713 K., Gorges, K., Heinze, R., Siligam, P. K., Burkhardt, U., Crewell, S., Hoose, C., Seifert, A., Tegen, I., and Quaas, J.: Detection

714 and attribution of aerosol–cloud interactions in large-domain large-eddy simulations with the ICOSahedral Non-hydrostatic
715 model, *Atmos. Chem. Phys.*, 20, 5657–5678, doi:10.5194/acp-20-5657-2020, 2020.

716

717 Delanoë, J., Heymsfield, A. J., Protat, A., Bansemmer, A., and Hogan, R. J.: Normalized particle size distribution for remote
718 sensing application, *J. Geophys. Res. Atmos.*, 119, 4204–4227, doi:10.1002/2013JD020700, 2014.

719

720 Diederich, M., Ryzhkov, A., Simmer, C., Zhang, P., and Trömel, S.: Use of specific attenuation for rainfall measurement at
721 X-band radar wavelengths - Part 1: Radar calibration and partial beam blockage estimation, *J. Hydrometeor.*, 16, 2, 487–502,
722 doi: 10.1175/JHM-D-14-0066.1, 2015a.

723

724 Diederich, M., Ryzhkov, A., Simmer, C., Zhang, P., and Trömel, S.: Use of specific attenuation for rainfall measurement at
725 X-band radar wavelengths - Part 2: Rainfall estimates and comparison with rain gauges, *J. Hydrometeor.*, 16, 2, 503–516, doi:
726 10.1175/JHM-D-14-0067.1, 2015b.

727

728 Dipankar, A., Stevens, B., Heinze, R., Moseley, C., Zängl, G., Giorgetta, M., and Brdar, S.: Large eddy simulations using the
729 general circulation model ICON, *J. Adv. Model. Earth Sy.*, 7, 963–986, doi.org/10.1002/2015MS000431, 2015.

730

731 Feng, Y., T. Janjic, Y. Zeng, A. Seifert, J. Min, 2021, Representing microphysical uncertainty in convective-scale data
732 assimilation using additive noise, *J. Adv. Model. Earth Sy.*, 2021 (submitted).

733

734 Field, P. R. and Heymsfield, A. J.: Importance of snow to global precipitation, *Geophys. Res. Lett.*, 42, 9512–9520,
735 doi:10.1002/2015GL065497, 2015.

736

737 Field, P. R., Lawson, R. P., Brown, P. R. A., Lloyd, G., Westbrook, C., Moisseev, D., Miltenberger, A., Nenes, A., Blyth, A.,
738 Chouarton, T., Connolly, P., Buehl, J., Crosier, J., Cui, Z., Dearden, C., DeMott, P., Flossmann, A., Heymsfield, A., Huang,
739 Y., Kalesse, H., Kanji, Z. A., Korolev, A., Kirchgaessner, A., Lasher-Trapp, S., Leisner, T., McFarquhar, G., Phillips, V.,
740 Stith, J., and Sullivan, S.: Secondary Ice Production: Current State of the Science and Recommendations for the Future,
741 *Meteorological Monographs*, 58, 7.1–7.20, doi: 10.1175/AMSMONOGRAPHS-D-16-0014.1, 2017

742 Forster, P., Storelvmo, T., Armour, K., Collins, W., Dufresne, J. L., Frame, D., Lunt, D. J., Mauritsen, T., Palmer, M. D.,
743 Watanabe, M., Wild, M., and Zhang, H.: The Earth’s Energy Budget, Climate Feedbacks, and Climate Sensitivity. In: *Climate*
744 *Change 2021: The Physical Science Basis. Contribution of Working Group I to the Sixth Assessment Report of the*
745 *Intergovernmental Panel on Climate Change*, Cambridge University Press, in press, 2021.

746

747 Frech, M., and Hubbert, J.: Monitoring the differential reflectivity and receiver calibration of the German polarimetric weather
748 radar network, *Atmos. Meas. Tech.*, 13, 1051–1069, doi: 10.5194/amt-13-1051-2020, 2020.

749

750 Gao, W., Sui, C.-H., Chen Wang, T.-C. and Chang, W.-Y.: An evaluation and improvement of microphysical parameterization
751 from a two-moment cloud microphysics scheme and the Southwest Monsoon Experiment (SoWMEX)/Terrain-influenced
752 Monsoon Rainfall Experiment (TiMREX) observations, *J. Geophys. Res. Atmos.*, 116, 1-13, doi:10.1029/2011JD015718,
753 2011.

754

755 Gasper, F., Görden, K., Shrestha, P., Sulis, M., Rihani, J., Geimer, M., and Kollet, S.: Implementation and scaling of the fully
756 coupled Terrestrial Systems Modeling Platform (TerrSysMP v1. 0) in a massively parallel supercomputing environment—a
757 case study on JUQUEEN (IBM Blue Gene/Q), *Geosci. Model Dev.*, 7(5), 2531-2543, 2014.

758

759 Gehring, J., Oertel, A., Vignon, E., Jullien, N., Besic, N., and Berne, A.: Microphysics and dynamics of snowfall associated
760 with a warm conveyor belt over Korea, *Atmos. Chem. Phys.*, 20, 7373–7392, doi: 10.5194/acp-20-7373-2020, 2020.

761

762 Grazioli, J., Tuia, D., and Berne, A.: Hydrometeor classification from polarimetric radar measurements: a clustering approach,
763 *Atmos. Meas. Tech.*, 8(1), 149-170, 2015.

764

765 Flamant, C., Knippertz, P., Fink, A.H., Akpo, A., Brooks, B., Chiu, C.J., Coe, H., Danuor, S., Evans, M., Jegede, O., Kalthoff,
766 N., Konaré, A., Lioussé, C., Lohou, F., Mari, C., Schlager, H., Schwarzenboeck, A., Adler, B., Amekudzi, L., Aryee, J.,
767 Ayoola, M., Batenburg, A.M., Bessardon, G., Borrmann, S., Brito, J., Bower, K., Burnet, F., Catoire, V., Colomb, A., Denjean,
768 C., Fosu-Amankwah, K., Hill, P.G., Lee, J., Lathon, M., Maranan, M., Marsham, J., Meynadier, R., Ngamini, J., Rosenberg,
769 P., Sauer, D., Smith, V., Stratmann, G., Taylor, J.W., Voigt, C., and Yoboué, V.: The Dynamics–Aerosol–Chemistry–Cloud
770 Interactions in West Africa Field Campaign: Overview and Research Highlights, *B. Am. Meteorol. Soc.*, 99, 83–
771 104,doi:10.1175/BAMS-D-16-0256.1, 2018

772

773 Fridlind, A. M., van Lier-Walqui, M., Collis, S., Giangrande, S. E., Jackson, R. C., Li, X., Matsui, T., Orville, R., Picel, M.
774 H., Rosenfeld, D., Ryzhkov, A., Weitz, R., and Zhang, P.: Use of polarimetric radar measurements to constrain simulated
775 convective cell evolution: a pilot study with Lagrangian tracking, *Atmos. Meas. Tech.*, 12, 2979–3000, doi:10.5194/amt-12-
776 2979-2019, 2019.

777

778 Hashino, T., and Tripoli, G. J.: The Spectral Ice Habit Prediction System (SHIPS). Part I: Model Description and Simulation
779 of the Vapor Deposition Process, *J. Atmos. Sci.*, 64(7), 2210-2237, doi:10.1175/JAS3963.1, 2007.

780

781 Heinze, R., Dipankar, A., Henken, C. C., Moseley, C., Sourdeval, O., Trömel, S., Xie, X., Adamidis, P., Ament, F., Baars, H.
782 Barthlott, C., Behrendt, A., Blahak, U., Bley, S., Brdar, S., Brueck, M., Crewell, S., Deneke, H., Girolamo, P. D., Evaristo,
783 R., Fischer, J., Frank, C., Friederichs, P., Göcke, T., Gorges, K., Hande, L., Hanke, M., Hansen, A., Hege, H.-C., Hoose, C.,
784 Jahns, T., Kalthoff, N., Klocke, D., Kneifel, S., Knippertz, P., Kuhn, A., Laar, T., Macke, A., Maurer, V., Mayer, B., Meyer,
785 C. I., Muppa, S. K., Neggers, R. A. J., Orlandi, E., Pantillon, F., Pospichal, B., Röber, N., Scheck, L., Seifert, A., Seifert, P.,
786 Senf, F., Siligam, P., Simmer, C., Steinke, S., Stevens, B., Wapler, K., Weniger, M., Wulfmeyer, V., Zängl, G., Zhang, D.,
787 and Quaas, J.: Large-eddy simulations over Germany using ICON: A comprehensive evaluation, *Q. J. Roy. Meteor. Soc.*, 143,
788 69-100, doi:10.1002/qj.2947, 2017.

789

790 Heymsfield, A., Bansemer, A., Wood, N. B., Liu, G., Tanelli, S., Sy, O. O., Poellot, M., and Liu, C.: Toward Improving Ice
791 Water Content and Snow-Rate Retrievals from Radars. Part II: Results from Three Wavelength Radar–Collocated In Situ
792 Measurements and CloudSat–GPM–TRMM Radar Data, *J. Appl. Meteor. Climatol.*, 57(2), 365-389. Retrieved Apr 6, 2021,
793 from <https://journals.ametsoc.org/view/journals/apme/57/2/jamc-d-17-0164.1.xml>, 2018.

794

795 [Hogan, R. J., Tian, L., Brown, P. R. A., Westbrook, C. D., Heymsfield, A. J., and Eastment, J. D.: Radar Scattering from Ice](#)
796 [Aggregates Using the Horizontally Aligned Oblate Spheroid Approximation, *J. Appl. Meteor. Climatol.*, 51\(3\), 655-671,](#)
797 [doi:10.1175/JAMC-D-11-074.1, 2012.](#)

798

799 Ilotoviz, E., Khain, A., Ryzhkov, A. V., and Snyder, J. C.: Relation between Aerosols, Hail Microphysics, and ZDR Columns,
800 *J. Atmos. Sci.*, 75, 1755-1781, doi:10.1175/JAS-D-17-0127.1, 2018.

801

802 Janjic, T., Bormann, N., Bocquet, M., Carton, J. A., Cohn, S. E., Dance, S. L., Losa, S. N., Nichols, N. K., Potthast, R., Waller,
803 J. A., and Weston, P.: On the representation error in data assimilation, *Q. J. R. Meteorol. Soc.*, 144:713, 1257-1278, 2018.

804

805 Jung, Y., Xue, M., Zhang, G., and Straka, J.: Assimilation of simulated polarimetric radar data for a convective storm using
806 ensemble Kalman filter. Part II: Impact of polarimetric data on storm analysis, *Mon. Wea. Rev.*, 136, 2246–2260,
807 [doi:10.1175/2007MWR2288.1](#), 2008.

808

809 Jung, Y., Xue, M., and Zhang, G.: Simultaneous Estimation of Microphysical Parameters and the Atmospheric State Using
810 Simulated Polarimetric Radar Data and an Ensemble Kalman Filter in the Presence of an Observation Operator Error, *Mon.*
811 *Wea. Rev.*, 138, 539–562, [doi:10.1175/2009MWR2748.1](#), 2010.

812

813 Jung, Y., Xue, M., and Tong, M.: Ensemble Kalman Filter Analyses of the 29—30 May 2004 Oklahoma Tornadoic
814 Thunderstorm Using One- and Two-Moment Bulk Microphysics Schemes, with Verification against Polarimetric Radar Data,
815 *Mon. Wea. Rev.*, 140, 1457-1475, doi: MWR-D-11-00032.1, 2012

816

817 Kalesse, H., Szyrmer, W., Kneifel, S., Kollias, P., and Luke, E.: Fingerprints of a riming event on cloud radar Doppler spectra:
818 observations and modeling, *Atmos. Chem. Phys.*, 16, 2997–3012, doi: 10.5194/acp-16-2997-2016, 2016.

819

820 Khain, A., Rosenfeld, D., and Pokrovsky, A.: Aerosol impact on the dynamics and microphysics of convective clouds, *Q. J.*
821 *R. Meteorol. Soc.*, 131, 2639–2663, doi:10.1256/qj.04.62, 2005.

822

823 Khain, A. P., Beheng, K. D., Heymsfield, A., Korolev, A., Krichak, S. O., Levin, Z., Pinsky, M., Phillips, V., Prabhakaran, T.,
824 Teller, A., et al.: Representation of microphysical processes in cloud-resolving models: Spectral (bin) microphysics versus
825 bulk parameterization, *Rev. Geophys.*, 53, 247– 322, doi:10.1002/2014RG000468, 2015.

826

827 Kleine, J., Voigt, C., Sauer, D., Schlager, H., Scheibe, M., Kaufmann, S. , Jurkat-Witschas, T., Kärcher, B., and Anderson B.:
828 In situ observations of ice particle losses in a young persistent contrail, *Geophys. Res. Lett.*, doi:10.1029/2018GL079390, 2018.

829

830 Kneifel S., A. von Lerber, J. Tiira, D. Moisseev, P. Kollias, and J. Leinonen: Observed Relations between Snowfall
831 Microphysics and Triple-frequency Radar Measurements, *J. Geophys. Res.*, 120, 6034-6055, doi: 10.1002/2015JD023156,
832 2015.

833

834 Kneifel, S., and Moisseev, D.: Long-term statistics of riming in non-convective clouds derived from ground-based Doppler
835 cloud radar observations, *J. Atmos. Sci.*, 77, 3495–3508, doi: 10.1175/JAS-D-20-0007.1, 2020.

836

837 Kollias, P., Albrecht, B.A., and Marks Jr F.: Why Mie? Accurate observations of vertical air velocities and raindrops using a
838 cloud radar. *Bulletin of the American Meteorological Society*, 83(10), 1471-1484, doi: 10.1175/BAMS-83-10-1471 2002

839

840 Kumjian, M.R.: Principles and applications of dual-polarization weather radar. Part I: Description of the polarimetric radar
841 variables. *J. Operational Meteor.*, 1(19), 226-242, doi: 10.15191/nwajom.2013.0119, 2013

842

843 Kumjian, M. R.: The impact of precipitation physical processes on the polarimetric radar variables, Dissertation, University
844 of Oklahoma, Norman Campus, <https://hdl.handle.net/11244/319188>, 2012

845

846 Kumjian, M. R., Khain, A. P., Benmoshe, N., Ilotoviz, E., Ryzhkov, A. V., and Phillips, V. T. J.: The anatomy and physics of
847 Z_{DR} columns: Investigating a polarimetric radar signature with a spectral bin microphysical model, *J. Appl. Meteor. Climatol.*,
848 53, 1820-1843, 2014.

849

850 Kumjian, M. R., Tobin, D. M., Oue, M., and Kollias, P.: Microphysical insights into ice pellet formation revealed by fully
851 polarimetric Ka-band Doppler radar, *J. Appl. Meteor. Climatol.*, 59, 1557–1580, doi: 10.1175/JAMC-D-20-0054.1, 2020.

852

853 Kuster, C. M., Schuur, T. J., Lindley, T. T., and Snyder, J. C.: Using ZDR Columns in Forecaster Conceptual Models and
854 Warning Decision-Making, *Weather and Forecasting*, 35(6), 2507-2522, 2020.

855

856 Le Treut, H. and Li, Z.-X.: Sensitivity of an atmospheric general circulation model to prescribed SST changes: Feedback
857 effects associated with the simulation of cloud optical properties, *Clim. Dyn.*, 5, 175–187, 1991.

858

859 Li, H., and Moisseev, D.: Two layers of melting ice particles within a single radar bright band: interpretation and implications,
860 *Geophys. Res. Lett.*, 47, e2020GL087499, doi: 10.1029/2020GL087499, 2020.

861

862 Libbrecht, K. G.: The physics of snow crystals, *Rep. Prog. Phys.*, 68, 855–895, doi:10.1088/0034-4885/68/4/R03, 2005.

863

864 Lohmann U. und E. Roeckner, Design and performance of a new cloud microphysics scheme developed for the ECHAM
865 general circulation model, *Clim. Dyn.*, 12, 557-572, 1996.

866

867 Lukach, M., Dufton, D., Crosier, J., Hampton, J.M., Bennett, L. and Neely III, R.R.. Hydrometeor classification of quasi-
868 vertical profiles of polarimetric radar measurements using a top-down iterative hierarchical clustering method. *Atmos. Meas.*
869 *Tech*, 14(2), pp.1075-1098, 2021

870

871 Luke E.P., Yang, F., Kollias, P., Vogelmann, A.M., Maahn, M.: New insights into ice multiplication using remote-sensing
872 observations of slightly supercooled mixed-phase clouds in the Arctic. *PNAS*, 118(13), e2021387118,
873 doi:10.1073/pnas.2021387118, 2021

874 Matrosov, S. Y., Reinking, R. F., Kropfli, R. A., Martner, B. E., and Bartram, B. W. (2001), On the use of radar depolarization
875 ratios for estimating shapes of ice hydrometeors in winter clouds, *Journal of Applied Meteorology*, 40, 479-490,
876 doi:10.1175/1520-0450(2001)040h0479:OTUORDi2.0.CO;2.

877

878 Matsui, T., Dolan, B., Rutledge, S. A., Tao, W.-K., Iguchi, T., Barnum, J., and Lang, S. E.: POLARRIS: A POLARimetric
879 Radar Retrieval and Instrument Simulator, *J. Geophys. Res.-Atmos.*, 124, 4634–4657, doi:10.1029/2018JD028317, 2019.

880

881 Mellado, J.P., Stevens, B., Schmidt, H., and Peters, N.: Buoyancy reversal in cloud-top mixing layers, *Q.J.R. Meteorol. Soc.*,
882 135: 963-978., doi:10.1002/qj.417, 2009.

883

884 Mendrok, J., Blahak, U., Snyder, J. C., and Carlin, J. T.: The polarimetric efficient modular volume scan radar forward operator
885 Pol-EMVORADO, *Geosci. Model Dev.*, 2021 (in preparation for this Special Issue).

886

887 Mishchenko, M. I.: Calculation of the amplitude matrix for a nonspherical particle in a fixed orientation, *Appl. Opt.* 39, 1026-
888 1031, 2000.

889

890 Moisseev, D. N., Lautaportti, S., Tyynela, J., and Lim, S.: Dualpolarization radar signatures in snowstorms: Role of snowflake
891 aggregation, *J. Geophys. Res. Atmos.*, 120, 12 644–12 655, doi:10.1002/2015JD023884, 2015.

892

893 Morrison, H. and Milbrandt, J. A.: Parameterization of Cloud Microphysics Based on the Prediction of Bulk Ice Particle
894 Properties. Part I: Scheme Description and Idealized Tests, *J. Atmos. Sci.*, 72(1), 287-311, 2015.

895

896 Morrison, H., van Lier-Walqui, M., Fridlind, A. M., Grabowski, W. W., Harrington, J. Y., and Hoose, C., et al.: Confronting
897 the challenge of modeling cloud and precipitation microphysics. *Journal of Advances in Modeling Earth Systems*, 12,
898 e2019MS001689. doi:10.1029/2019MS001689, 2020.

899

900 Mülmenstädt, J., Sourdeval, O., Delanoë, J., and Quaas, J.: Frequency of occurrence of rain from liquid-, mixed- and ice-phase
901 clouds derived from A-Train satellite retrievals, *Geophys. Res. Lett.*, 42, 6502-6509, doi:10.1002/2015GL064604, 2015.

902 Murphy, A. M., Ryzhkov, A., & Zhang, P.: Columnar vertical profile (CVP) methodology for validating polarimetric radar
903 retrievals in ice using in situ aircraft measurements. *J. Atmos. Oceanic Technol.*, 37(9), 1623-1642, doi:10.1175/JTECH-D-
904 20-0011.1, 2020.

905

906 Myagkov, A., Seifert, P., Bauer-Pfundstein, M., and Wandinger, U.: Cloud radar with hybrid mode towards estimation of
907 shape and orientation of ice crystals, *Atmos. Meas. Tech.*, 9, 469–489, doi:10.5194/amt-9-469-2016, 2016.

908

909 Neggers, R. A.: A dual mass flux framework for boundary layer convection. Part II: Clouds, *J. Atmos. Sci.*, 66, 1489–1506,
910 doi:10.1175/2008JAS2636.1, 2009.

911
912 Neto, J. D., Kneifel, S., Ori, D., Trömel, S., Handwerker, J., Bohn, B., Hermes, N., Mühlbauer, K., Lenefer, M., and Simmer,
913 C.: The TRIPLE-frequency and Polarimetric radar Experiment for improving process observation of winter precipitation. *Earth*
914 *Syst. Sci. Data*, 11, 845–863, [doi: 10.5194/essd-11-845-2019](https://doi.org/10.5194/essd-11-845-2019), 2019.

915
916 Nguyen, C., Wolde, M., Baibakov, K., and Korolev, A.: Detection and estimation of high ice water content using X- and W-
917 band dual-polarization airborne radar data, 38th Conf. on Radar Meteorology, Chicago, IL, Amer. Meteor. Soc., 89,
918 <https://ams.confex.com/ams/38RADAR/webprogram/Paper321101.html>, 2017.

919
920 Nguyen, C. M., Wolde, M., and Korolev, A.: Determination of ice water content (IWC) in tropical convective clouds from X-
921 band dual-polarization airborne radar, *Atmos. Meas. Tech.*, 12, 5897–5911, [doi: 10.5194/amt-12-5897-2019](https://doi.org/10.5194/amt-12-5897-2019), 2019.

922
923 Ori, D., V. Schemann, M. Karrer, J. Dias Neto, L. von Terzi, A. Seifert, and S. Kneifel: Evaluation of ice particle growth in
924 ICON using statistics of multi-frequency Doppler cloud radar observations, *Q. J. Roy. Meteor. Soc.*, 146: 3830– 3849.
925 [doi:10.1002/qj.3875](https://doi.org/10.1002/qj.3875), 2020

926 Oue, M., A. Tatarevic, P. Kollias, D. Wang, K. Yu, and A.M. Vogelmann: The Cloud-resolving model Radar SIMulator (CR-
927 SIM) Version 3.3: description and applications of a virtual observatory, *Geoscientific Model Development*, 13: 1975-1998.
928 [doi: 10.5194/gmd-13-1975-2020](https://doi.org/10.5194/gmd-13-1975-2020), 2020.

929 Oue, M., Kollias, P., Ryzhkov, A., and Luke, E. P.: Toward exploring the synergy between cloud radar polarimetry and Doppler
930 spectral analysis in deep cold precipitating systems in the Arctic, *J. Geophys. Res. Atmos.*, 123, 2797–2815, [doi:](https://doi.org/10.1002/2017JD027717)
931 [10.1002/2017JD027717](https://doi.org/10.1002/2017JD027717), 2018.

932 Phillips, V. T. J., Yano, J., & Khain, A. (2017). Ice Multiplication by Breakup in Ice–Ice Collisions. Part I: Theoretical
933 Formulation, *J. Atmos. Sci.*, 74(6), 1705-1719

934 Pfitzenmayer L., Unal, C. M. H., Dufournet, Y., Ruschenberg, H. W. J.: Observing ice particle growth along fall streaks in
935 mixed-phase clouds using spectral polarimetric radar data, *Atmos. Chem. Phys.*, 18, 7843-7863, [doi: 10.5194/acp-18-7843-](https://doi.org/10.5194/acp-18-7843-2018)
936 [2018](https://doi.org/10.5194/acp-18-7843-2018), 2018.

937 Pincus, R. and Klein, S.: Unresolved spatial variability and microphysical process rates in large-scale models, *J. Geophys.*
938 *Res.*, 105, 27059 - 27065, 2000.

939

940 Putnam, B., Xue, M., Jung, Y., Snook, N., and Zhang, G.: Ensemble Kalman Filter Assimilation of Polarimetric Radar
941 Observations for the 20 May 2013 Oklahoma Tornadoic Supercell Case, *Mon. Wea. Rev.*, 147, 2511–2533, [doi:10.1175/MWR-](https://doi.org/10.1175/MWR-D-18-0251.1)
942 [D-18-0251.1](https://doi.org/10.1175/MWR-D-18-0251.1), 2019.

943

944 Radenz, M., Bühl, J., Seifert, P., Baars, H., Engelmann, R., Barja González, B., Mamouri, R.-E., Zamorano, F., and Ansmann,
945 A.: Hemispheric contrasts in ice formation in stratiform mixed-phase clouds: Disentangling the role of aerosol and dynamics
946 with ground-based remote sensing, *Atmos. Chem. Phys. Discuss.* [preprint], <https://doi.org/10.5194/acp-2021-360>, in review,
947 2021.

948

949 Reimann, L., Simmer, C., and Trömel, S.: Dual-polarimetric radar estimators of liquid water content over Germany, Accepted
950 for *Meteorol. Z. (Contrib. Atm. Sci.)*, doi:[10.1127/metz/2021/1072](https://doi.org/10.1127/metz/2021/1072), 2021.

951

952 Ribaud, J.-F., L. A. T. Machado, and T. Biscaro: X-band dual-polarization radar-based hydrometeor classification for Brazilian
953 tropical precipitation systems, *Atmos. Meas. Tech.*, 12, 811–837, doi.org/10.5194/amt-12-811-2019, 2019.

954

955 Rosch, J., et al.: Analysis of diagnostic climate model cloud parameterisations using large-eddy simulations, *Q. J. R. Meteorol.*
956 *Soc.*, 141, 2199-2205, doi:10.1002/qj.2515, 2015.

957

958 Rotstajn, L. D.: On the tuning of autoconversion parameterizations in climate models, *J. Geophys. Res.*, 105, 15,495–15,507,
959 2000.

960

961 Ryzhkov, A. V., Zrníc, D. S., and Gordon, B. A.: Polarimetric Method for Ice Water Content Determination, *J. Appl. Meteor.*
962 *Climatol.*, 37, 125-134, 1998.

963

964 Ryzhkov, A., Pinsky, M., Pokrovsky, A., and Khain, A.: Polarimetric Radar Observation Operator for a Cloud Model with
965 Spectral Microphysics, *J. Appl. Meteor. Climatol.*, 50, 873-894, 2011.

966

967 Ryzhkov, A., Zhang, P., Reeves, H., Kumjian, M., Tschallener, T., Trömel, S., and Simmer, C.: Quasi-vertical profiles – a
968 new way to look at polarimetric radar data, *J. Atmos. Oceanic Technol.*, 33, 551-562, [doi: 10.1175/JTECH-D-15-0020.1](https://doi.org/10.1175/JTECH-D-15-0020.1), 2016.

969

970 Ryzhkov, A., Bukovcic, P., Murphy, A., Zhang, P., and McFarquhar, G.: Ice Microphysical Retrievals Using Polarimetric
971 Radar Data. In *Proceedings of the 10th European Conference on Radar in Meteorology and Hydrology*, Ede, The Netherlands,
972 1–6 July 2018.

973

974 Ryzhkov, A. and Zrnica, D.: Radar Polarimetry for Weather Observations, Springer Atmospheric Sciences, 486 pp., 2019.
975

976 Schinagl, K., Friederichs, P., Trömel, S., and Simmer, C.: Gamma Drop Size Distribution Assumptions in Bulk Model
977 Parameterizations and Radar Polarimetry and Their Impact on Polarimetric Radar Moments, *J. Appl. Meteor. Climatol.*, 58,
978 467–478, [doi: 10.1175/JAMC-D-18-0178.1](https://doi.org/10.1175/JAMC-D-18-0178.1), 2019.
979

980 Schrom, R. S. and Kumjian, M. R.: Bulk-Density Representations of Branched Planar Ice Crystals: Errors in the Polarimetric
981 Radar Variables, *J. Appl. Meteor. Climatol.*, 57(2), 333-346, 2018.
982

983 Seifert, A. and Beheng, K. D.: A two-moment cloud microphysics parameterization for mixed-phase clouds. Part 1: Model
984 description, *Meteorol. Atmos. Phys.*, 92, 45-66, [doi: 10.1007/s00703-005-0112-4](https://doi.org/10.1007/s00703-005-0112-4), 2006.

985 Shrestha, P., Sulis, M., Masbou, M., Kollet, S. and Simmer, C.: A scale-consistent Terrestrial System Modeling Platform based
986 on COSMO, CLM and ParFlow, *Mon. Wea. Rev.*, 142, 3466-3483, [doi: 10.1175/MWR-D-14-00029.1](https://doi.org/10.1175/MWR-D-14-00029.1), 2014

987 Shrestha, P.: Clouds and vegetation modulate shallow groundwater table depth, 22, 753 – 763, [doi:10.1175/JHM-D-20-0171.1](https://doi.org/10.1175/JHM-D-20-0171.1),
988 2021

989 Shrestha, P., Trömel, S., Evaristo, R., and Simmer, C.: Evaluation of modeled summertime convective storms using
990 polarimetric radar observations, *Atmos. Chem. Phys. Discuss.* [preprint], <https://doi.org/10.5194/acp-2021-404>, in review,
991 2021a.

992 Shrestha, P., Mendrok, J., Pejčic, V., Trömel, S., and Blahak, U.: The impact of uncertainties in model microphysics, retrievals
993 and forward operators on model evaluations in polarimetric radar space, *Geosci. Model Dev.*, 2021b (submitted).
994

995 Shupe, M. D., Kollias, P., Matrosov, S. Y., and Schneider, T. L.: Deriving mixed-phase cloud properties from Doppler radar
996 spectra, *J. Atmos. Oceanic Technol.*, 21, 660–670, [doi: 10.1175/1520-0426\(2004\)021<0660:DMCPFD>2.0.CO;2](https://doi.org/10.1175/1520-0426(2004)021<0660:DMCPFD>2.0.CO;2), 2004.
997

998 Simmel, M., Bühl, J., Ansmann, A., and Tegen, I.: Ice phase in altocumulus clouds over Leipzig: remote sensing observations
999 and detailed modeling, *Atmos. Chem. Phys.*, 15, 10453–10470, [doi:10.5194/acp-15-10453-2015](https://doi.org/10.5194/acp-15-10453-2015), 2015.
1000

1001 Simmer, C., Thiele-Eich, I., Masbou, M., Amelung, W., Crewell, S., Diekkruöger, B., Ewert, F., Hendricks Franssen, H.-J.,
1002 Huisman, A. J., Kemna, A., Klitzsch, N., Kollet, S., Langensiepen, M., Löhnert, U., Rahman, M., Rascher, U., Schneider, K.,
1003 Schween, J., Shao, Y., Shrestha, P., Stiebler, M., Sulis, M., Vanderborght, J., Vereecken, H., van der Kruk, J., Zerenner, T.,
1004 and Waldhoff, G.: Monitoring and Modeling the Terrestrial System from Pores to Catchments - the Transregional

1005 Collaborative Research Center on Patterns in the Soil-Vegetation-Atmosphere System, B. Am. Meteorol. Soc., 96, 1765–1787,
1006 doi: 10.1175/BAMS-D-13-00134.1, 2015.

1007

1008 Simmer, C., Adrian, G., Jones, S., Wirth, V., Goeber, M., Hohenegger, C., Janjic, T., Keller, J., Ohlwein, C., Seifert, A.,
1009 Trömel, S., Ulbrich, T., Wapler, K., Weissmann, M., Keller, J., Masbou, M., Meilinger, S., Riss, N., Schomburg, A., Vormann,
1010 A., and Weingaertner, C.: HErZ - The German Hans-Ertel Centre for Weather Research. B. Am. Meteorol. Soc., 1057-1068,
1011 doi: [10.1175/BAMS-D-13-00227.1](https://doi.org/10.1175/BAMS-D-13-00227.1), 2014

1012

1013 Smith, R. N.: A scheme for predicting layer clouds and their water content in a general circulation model, Q. J. R. Meteorol.
1014 Soc., 116, 435–460, doi:10.1002/qj.49711649210, 1990.

1015

1016 Snyder, J.C., Ryzhkov, A.V., Kumjian, M.R., Khain, A.P., and Picca, J.C.: A ZDR column detection algorithm to examine
1017 convective storm updrafts, Weather and Forecasting, 30, 1819-1844, 2015.

1018

1019 Sommeria, G. and Deardorff, J. W.: Subgrid-scale condensation models of non-precipitating clouds, J. Atmos. Sci., 34, 344-
1020 355, 1977.

1021

1022 Sourdeval, O., Gryspeerd, E., Krämer, M., Goren, T., Delanoë, J., Afchine, A., Hemmer, F., and Quaas, J.: Ice crystal number
1023 concentration estimates from lidar–radar satellite remote sensing – Part 1: Method and evaluation, Atmos. Chem. Phys., 18,
1024 14327–14350, doi: [10.5194/acp-18-14327-2018](https://doi.org/10.5194/acp-18-14327-2018), 2018.

1025

1026 Spek, A. L. J., Unal, C. M. H., Moisseev, C. N., Russchenberg, H. W. J., Chandrasekar, V., Dufournet, Y.: A New Techniques
1027 to Categorize and Retrieve the Microphysical Properties of Ice Particles above the Melting Layer Using Radar Dual-
1028 Polarization Spectral Analysis, Jtech, doi: 10.1175/2007JTECHA944.1, 2008.

1029

1030 Stevens, B., Acquistapace, C., Hansen, A., Heinze, R., Klinger, C., Klocke, D., Schubotz, W., Windmiller, J., Adamidis, P.,
1031 Arka, I., Barlakas, V., Biercamp, J., Brueck, M., Brune, S., Buehler, S., Burkhardt, U., Cioni, G., Costa-Surós, M., Crewell,
1032 S., Crueger, T., Deneke, H., Friederichs, P., Carbajal Henken, C., Hohenegger, C., Jacob, M., Jakub, F., Kalthoff, N., Köhler,
1033 M., Van Laar, T. W., Li, P., Löhnert, U., Macke, A., Madenach, N., Mayer, B., Nam, C., Naumann, A. K., Peters, K., Poll, S.
1034 , Quaas, J., Röber, N., Rochetin, N., Rybka, H., Scheck, L., Schemann, V., Schnitt, S., Seifert, A., Senf, F., Shapkalijevski,
1035 M., Simmer, C., Singh, S., Sourdeval, O., Spickermann, D., Strandgren, J., Tessiot, O., Vercauteren, N., Vial, J., Voigt, A.,
1036 and Zängl, G.: Large-eddy and storm resolving models for climate prediction - the added value for clouds and precipitation, J.
1037 Meteorol. Soc. Japan, 98, doi:10.2151/jmsj.2020-021, 2020.

1038

1039 Stevens, B., et al.: Atmospheric component of the MPI-M Earth System Model: ECHAM6, *J. Adv. Model. Earth Syst.* 5: 146–
1040 172, doi: 10.1002/jame.20015, 2013.

1041

1042 Stevens, B. and Feingold, G.: Untangling Aerosol Effects on Clouds and Precipitation in a Buffered System, *Nature*, 461, 607–
1043 613, 2009.

1044

1045 Sundqvist, H., et al., Condensation and cloud parameterization studies with a mesoscale numerical weather prediction model,
1046 *Mon. Weather Rev.*, 117, 1641–1657, 1989.

1047

1048 Takahashi, T.: High ice crystal production in winter cumuli over the Japan Sea, *Geophysical research letters*, 20.6, 451–454,
1049 1993.

1050

1051 Takahashi, T., Yoshihiro N., and Yuzuru K.: Possible high ice particle production during graupel–graupel collisions, *J. Atmos.*
1052 *Sci.*, 52.24, 4523–4527, 1995.

1053

1054 Takahashi, T.: Influence of liquid water content and temperature on the form and growth of branched planar snow crystals in
1055 a cloud, *J. Atmos. Sci.*, 71.11, 4127–4142, 2014.

1056

1057 Tiedtke, M.: Representation of clouds in large scale models, *Mon. Weather Rev.*, 121, 3040–3061, 1993.

1058

1059 Tompkins, A.: A prognostic parameterization for the subgrid-scale variability of water vapor and clouds in large-scale models
1060 and its use to diagnose cloud cover, *J. Atmos. Sci.*, 59:1917–1942, 2002.

1061

1062 Trömel, S., Quaas, J., Crewell, S., Bott, A., and Simmer, C.: Polarimetric Radar Observations Meet Atmospheric Modelling.
1063 19th International Radar Symposium (IRS), Bonn, doi: 10.23919/IRS.2018.8448121, 2018.

1064

1065 Trömel, S., Ryzhkov, A. V., Hickman, B., Mühlbauer, K., and Simmer, C.: Polarimetric Radar Variables in the Layers of
1066 Melting and Dendritic Growth at X Band—Implications for a Nowcasting Strategy in Stratiform Rain, *J. Appl. Meteor.*
1067 *Climatol.*, 58, 2497–2522, doi:10.1175/JAMC-D-19-0056.1, 2019.

1068

1069 Trömel, S., A. V. Ryzhkov, P. Zhang, and C. Simmer: The microphysical information of backscatter differential phase δ in the
1070 melting layer, *J. Appl. Meteor. Climatol.*, 53, 2344–2359, 2014.

1071

1072 Verlinde, J., Rambukkange, M. P., Clothiaux, E. E., McFarquhar, G. M., and Eloranta, E. W.: Arctic multilayered, mixed-
1073 phase cloud processes revealed in millimeter-wave cloud radar Doppler spectra, *J. Geophys. Res. Atmos.*, 118, 13199–13213,
1074 doi: 10.1002/2013JD020183, 2013.

1075

1076 Vogl, T., Maahn, M., Kneifel, S., Schimmel, W., Moisseev, D., and Kalesse-Los, H.: Using artificial neural networks to predict
1077 riming from Doppler cloud radar observations, *Atmos. Meas. Tech. Discuss.* [preprint], <https://doi.org/10.5194/amt-2021-137>,
1078 in review, 2021.

1079

1080 Voigt, C., Schumann, U., Jurkat, T., Schäuble, D., Schlager, H., Petzold, A., Gayet, J.-F., Krämer, M., Schneider, J., Borrmann,
1081 S., Schmale, J., Jessberger, P., Hamburger, T., Lichtenstern, M., Scheibe, M., Gourbeyre, C., Meyer, J., Kübbeler, M., Frey,
1082 W., Kalesse, H., Butler, T., Lawrence, M. G., Holzäpfel, F., Arnold, F., Wendisch, M., Döpelheuer, A., Gottschaldt, K.,
1083 Baumann, R., Zöger, M., Sölch, I., Rautenhaus, M., and Dörnbrack, A.: In-situ observations of young contrails – overview
1084 and selected results from the CONCERT campaign, *Atmos. Chem. Phys.*, 10, 9039–9056, doi:10.5194/acp-10-9039-2010,
1085 2010.

1086

1087 Voigt, C., Jeßberger, P., Jurkat, T., Kaufmann, S., Baumann, R., Schlager, H., Bobrowski, N., Guffirda, G., and Salerno, G.:
1088 Evolution of CO₂, SO₂, HCl and HNO₃ in the volcanic plumes from Etna, *Geophys. Res. Lett.*, 41,
1089 doi:10.1002/2013GL058974, 2014.

1090

1091 Voigt, C., Schumann, U., Minikin, A., Abdelmonem, A., Afchine, A., Borrmann, S., Boettcher, M., Buchholz, B., Bugliaro,
1092 L., Costa, A., Curtius, J., Dollner, M., Dörnbrack, A., Dreiling, V., Ebert, V., Ehrlich, A., Fix, A., Forster, L., Frank, F.,
1093 Fütterer, D., Giez, A., Graf, K., Groß, J., Groß, S., Heimerl, K., Heinold, B., Hüneke, T., Järvinen, E., Jurkat, T., Kaufmann,
1094 S., Kenntner, M., Klingebiel, M., Klimach, T., Kohl, R., Krämer, M., Krisna, T. C., Luebke, A., Mayer, B., Mertens, S.,
1095 Molleker, S., Petzold, A., Pfeilsticker, K., Port, M., Rapp, M., Reutter, P., Rolf, C., Rose, D., Sauer, D., Schäfler, A., Schlage,
1096 R., Schnaiter, M., Schneider, J., Spelten, N., Spichtinger, P., Stock, P., Walser, A., Weigel, R., Weinzierl, B., Wendisch, M.,
1097 Werner, F., Wernli, H., Wirth, M., Zahn, A., Ziereis, H., and Zöger, M.; ML-CIRRUS: The Airborne Experiment on Natural
1098 Cirrus and Contrail Cirrus with the High-Altitude Long-Range Research Aircraft HALO, *B. Am. Meteorol. Soc.* 98(2), 271-
1099 288, doi:[bams-d-15-00213.1](https://doi.org/10.1175/BAMS-D-15-00213.1), 2017.

1100 Voigt, C., Lelieveld, J., Schlager, H., Schneider, J., Sauer, D., Meerkötter, R., Pöhlker, M., Bugliaro, L., Curtius, J.,
1101 Erbertseder, T., Hahn, V., Jöckel, P., Li, Q., Marsing, A., Mertens, M., Pöhlker, C., Pöschl, U., Pozzer, A., Tomsche, L., and
1102 Schumann, U.: Aerosol and Cloud Changes during the Corona Lockdown in 2020 - First highlights from the BLUESKY
1103 campaign; EGU21-13134, <https://meetingorganizer.copernicus.org/EGU21/session/40818>, 2021.

1104 Wang, M., Zhao, K., Pan, Y., Xue, M.: Evaluation of simulated drop size distributions and microphysical processes using
1105 polarimetric radar observations for landfalling Typhoon Matmo (2014), *J. Geophys. Res. Atmos.*, 125, 1-20,
1106 doi:10.1029/2019JD031527, 2020.

1107 Weissmann, M., M. Göber, C. Hohenegger, T. Janjic, J. Keller, C. Ohlwein, A. Seifert, S. Trömel, T. Ulbrich, K. Wapler, C.
1108 Bollmeyer, H. Deneke: The Hans-Ertel Centre for Weather Research – Research objectives and highlights from its first three
1109 years. *Meteorol. Z.*, 23(3), 193 – 208, 2014.

1110 Wendisch, M., Pöschl, U., Andreae, M. O., Machado, L. A. T., Albrecht, R., Schlager, H., Rosenfeld, D., Martin, S. T.,
1111 Abdelmonem, A., Afchine, A., Araùjo, A. C., Artaxo, P., Aufmhoff, H., Barbosa, H. M. J., Borrmann, S., Braga, R., Buchholz,
1112 B., Cecchini, M. A., Costa, A., Curtius, J., Dollner, M., Dorf, M., Dreiling, V., Ebert, V., Ehrlich, A., Ewald, F., Fisch, G.,
1113 Fix, A., Frank, F., Fütterer, D., Heckl, C., Heidelberg, F., Hüneke, T., Jäkel, E., Järvinen, E., Jurkat, T., Kanter, S., Kästner,
1114 U., Kenntner, M., Kesselmeier, J., Klimach, T., Knecht, M., Kohl, R., Kölling, T., Krämer, M., Krüger, M., Krisna, T. C.,
1115 Lavric, J. V., Longo, K., Mahnke, C., Manzi, A. O., Mayer, B., Mertes, S., Minikin, A., Molleker, S., Münch, S., Nillius, B.,
1116 Pfeilsticker, K., Pöhlker, C., Roiger, A., Rose, D., Rosenow, D., Sauer, D., Schnaiter, M., Schneider, J., Schulz, C., de Souza,
1117 R. A. F., Spanu, A., Stock, P., Vila, D., Voigt, C., Walser, A., Walter, D., Weigel, R., Weinzierl, B., Werner, F., Yamasoe, M.
1118 A., Ziereis, H., Zinner, T., and Zöger, M.: ACRIDICON–CHUVA Campaign: Studying Tropical Deep Convective Clouds and
1119 Precipitation over Amazonia Using the New German Research Aircraft HALO, *B. Am. Meteorol. Soc.*, 97(10), 1885-1908,
1120 doi:[bams-d-14-00255.1](https://doi.org/10.1175/BAMS-D-14-00255.1), 2016.

1121 Wolfensberger, D. and Berne, A.: From model to radar variables: a new forward polarimetric radar operator for COSMO,
1122 *Atmos. Meas. Tech.*, 11, 3883-3916, doi: 10.5194/amt-11-3883-2018, 2018.

1123 Xie, X., Evaristo, R., Trömel, S., Saavedra, P., Simmer, C., and Ryzhkov, A.: Radar Observation of Evaporation and
1124 Implications for Quantitative Precipitation and Cooling Rate Estimation, *J. Atmos. Oceanic Technol.* 33(8), 1779-1792,
1125 doi:[10.1175/JTECH-D-15-0244.1](https://doi.org/10.1175/JTECH-D-15-0244.1), 2016.

1126

1127 Xie, X., Shrestha, P., Mendrok, J., Carlin, J., Trömel, S., and Blahak, U.: Bonn Polarimetric Radar forward Operator (B-PRO),
1128 CRC/TR32 Database (TR32DB), doi:10.5880/TR32DB.41, 2021, (accessed 8 April 2021).

1129

1130 Xue, L., Fan, J., Lebo, Z. J., Wu, W., Morrison, H., Grabowski, W. W., Chu, X., Geresdi, I., North, K., Stenz, R., Gao, Y.,
1131 Lou, X., Bansemer, A., Heymsfield, A. J., McFarquhar, G. M., and Rasmussen, R. M.: Idealized Simulations of a Squall Line
1132 from the MC3E Field Campaign Applying Three Bin Microphysics Schemes: Dynamic and Thermodynamic Structure,
1133 *Monthly Weather Review*, 145(12), 4789-4812, doi:10.1175/MWR-D-16-0385.1, 2017.

1134

1135 You, C.-R., Chung, K.-S., and Tsai, C.-C.: Evaluating the performance of convection-permitting model by using dual-
1136 polarimetric radar parameters: Case study of SoWMEX IOP8, *Remote Sensing*, 12(18):3004, 1-25, doi:10.3390/rs12183004,
1137 2020.

1138

1139 Zängl, G., et al.: The ICON (icosahedral non-hydrostatic) modelling framework of DWD and MPI-M: Description of the non-
1140 hydrostatic dynamical core, *Q. J. Roy. Meteor. Soc.*, 141, 563–579, 2015.

1141

1142 Zeng, Y., Janjic, T., Lozar, A. de, Welzbacher, C. A., Blahak, U., and Seifert, A.: Assimilating radar radial wind and reflectivity
1143 data in an idealized setup of the COSMO-KENDA system, *Atmospheric Research*, 249, 105282,
1144 [doi:10.1016/j.atmosres.2020.105282](https://doi.org/10.1016/j.atmosres.2020.105282), 2021a.

1145

1146 Zeng, Y., Janjic, T., Feng, Y., Blahak, U., de Lozar, A., Bauernschubert, E., Stephan, K., and Min, J.: Interpreting estimated
1147 observation error statistics of weather radar measurements using the ICON-LAM-KENDA system, *Atmos. Meas. Tech.*, 14,
1148 5735–5756, <https://doi.org/10.5194/amt-14-5735-2021>, 2021b.

1149

1150 Zeng, Y., Janjic, T., Lozar, A. de, Rasp, S., Blahak, U., Seifert, A., and Craig, G. C.: Comparison of methods accounting for
1151 subgrid-scale model error in convective-scale data assimilation, *Mon. Wea. Rev.*, 148, 2457-2477, 2020.

1152

1153 Zeng Y., Janjic, T., Sommer, M., Lozar, A. de, Blahak, U., and Seifert, A.: Representation of model error in convective-scale
1154 data assimilation: additive noise based on model truncation error, *J. Adv. Model. Earth Sy.*, 11, 752-770, 2019.

1155

1156 Zeng, Y., Janjic, T., Lozar, A. de, Blahak, U., Reich, H., Keil, C., and Seifert, A.: Representation of model error in convective-
1157 scale data assimilation: Additive noise, relaxation methods and combinations, *J. Adv. Model. Earth Sy.*, 10, 2889–2911, 2018.

1158

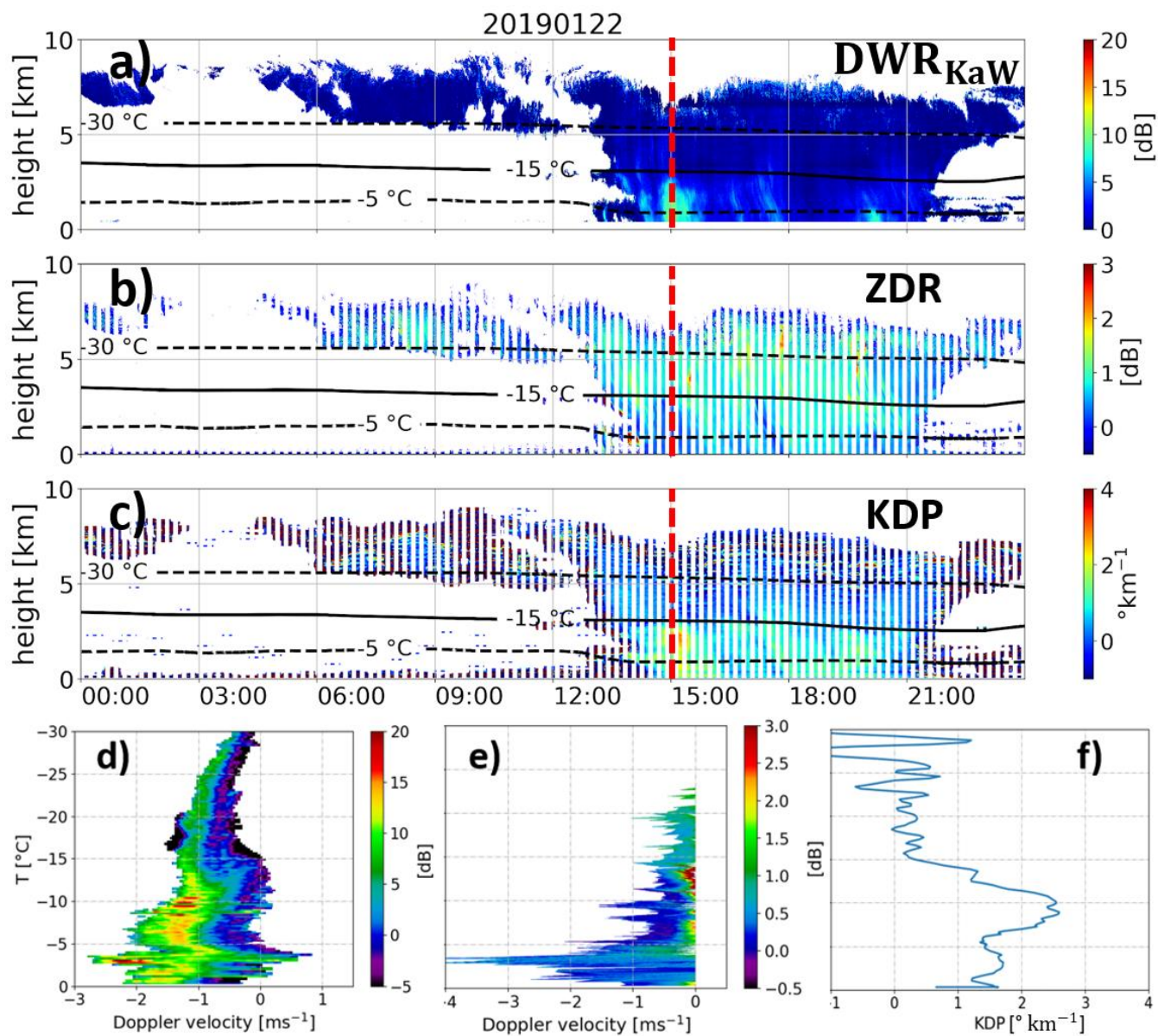
1159 Zeng, Y., Blahak, U., and Jerger, D.: An efficient modular volume-scanning radar forward operator for NWP models:
1160 description and coupling to the COSMO model, *Q. J. Roy. Meteor. Soc.*, 142(701), 3234-3256, 2016

1161

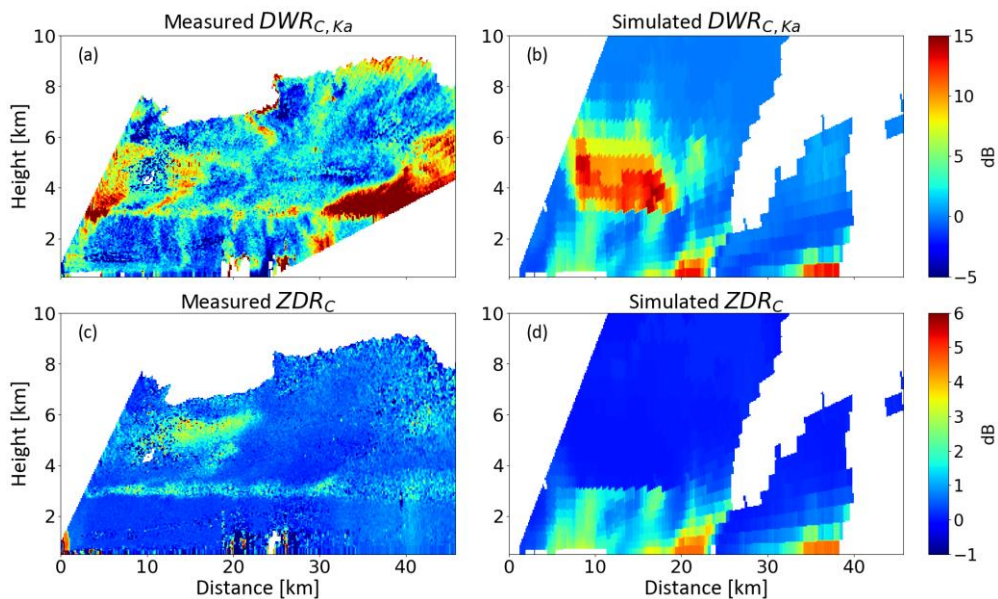
1162 Zhu, K., Xue, M., Ouyang, K., and Jung, Y.: Assimilating polarimetric radar data with an ensemble Kalman filter: OSSEs with
1163 a tornadic supercell storm simulated with a two-moment microphysics scheme, *Q. J. Roy. Meteor. Soc.*, 146: 1880– 1900,
1164 [doi:10.1002/qj.3772](https://doi.org/10.1002/qj.3772), 2020.

1165

1166

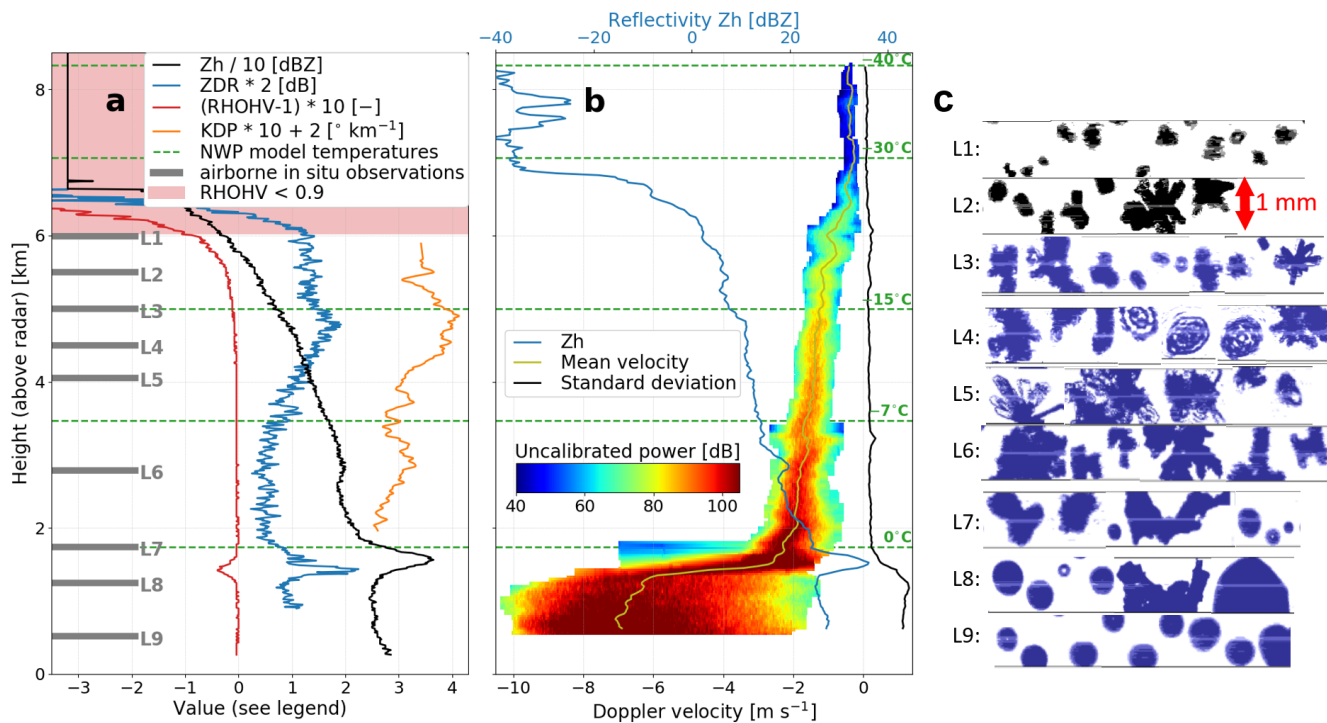


1167
 1168 **Figure 1: Observations at JOYCE-CF shows a) DWR_{KaW}, b) Z_{DR} (measured at a 30° elevation angle), c) K_{DP} (also measured at 30°**
 1169 **elevation angle) on 22 January 2019. Panels d)-f) show the observed DWR-spectrum, Z_{DR}-spectrum and K_{DP}-profile at 15:00 UTC**
 1170 **(indicated by the red line in panels a)-c))**



1175

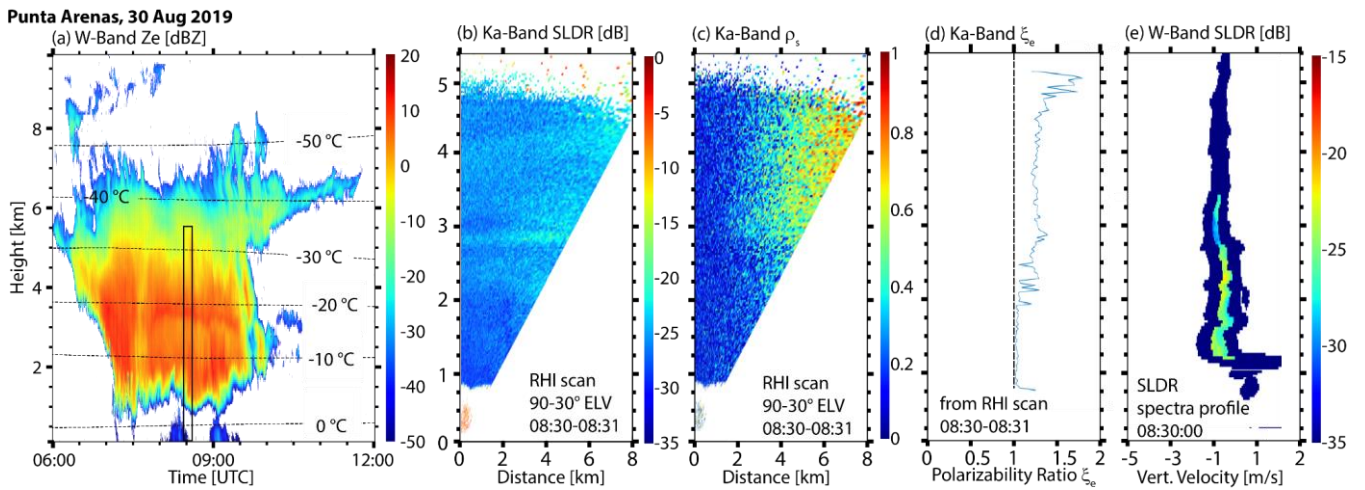
1176 **Figure 2** (a) Dual-wavelength ratio between the C-band POLDIRAD and Ka-band miraMACS measurements on the 7th July 2019,
 1177 (b) simulated dual-wavelength ratio, (c) differential radar reflectivity ZDR measured by the C-band radar POLDIRAD, and (d)
 1178 simulated ZDR of a comparable, but not identical, precipitation event using the P3 scheme (Morrison and Milbrandt, 2015).



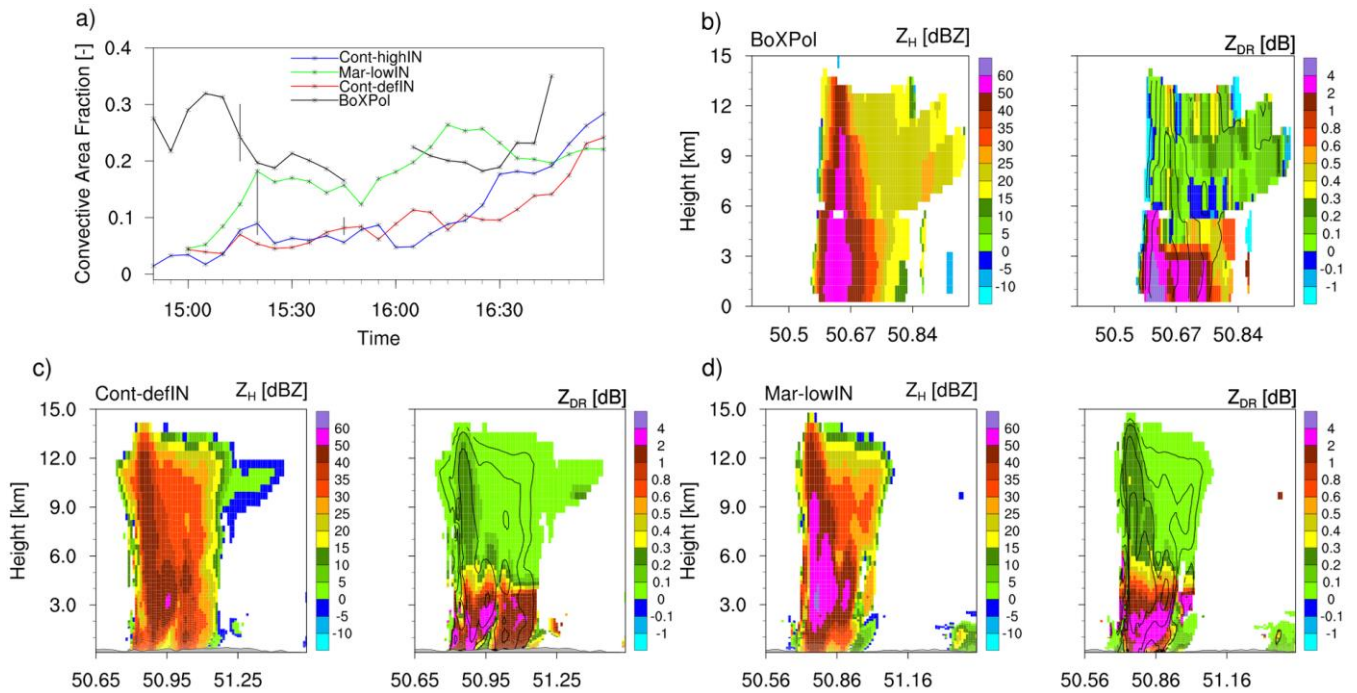
1179

1180 **Figure 3:** Measurements of slant-viewing and zenith-pointing polarimetric C-band weather radar scans with NWP model based
 1181 temperature levels and airborne in-situ observations: (a) quasi-vertical profiles (QVPs) of radar reflectivity Z_H , differential
 1182 reflectivity Z_{DR} , copolar cross-channel correlation coefficient ρ_{HV} , and the specific differential phase K_{DP} estimated from (noisy)
 1183 measurements of the differential phase by aggressive filtering above the melting layer; (b) average Doppler spectra from a 15 s
 1184 birdbath scan and corresponding first 3 moments at each radar bin height: reflectivity, power-weighted mean velocity and standard
 1185 deviation; (c) in situ particle images (downward-looking projection images) collected at altitudes L1 to L9.

1186
 1187
 1188
 1189



1190
 1191 **Figure 4:** Case study of a deep mixed-phase cloud event observed with multiwavelength polarimetric cloud radars at Punta Arenas,
 1192 Chile, on 30 August 2019. (a) vertical-pointing W-Band (94-GHz) radar reflectivity factor Z_e and isolines of modeled air
 1193 temperature, (b) and (c) Ka-Band (35-GHz) RHI scans (90° - 30° elevation) of slanted linear depolarization ratio SLDR and co-cross
 1194 correlation coefficient in the slanted basis ρ_s , respectively, from 08:30-08:31 UTC, (d) profile of the shape index polarizability ratio
 1195 (ξ_e) obtained from the RHI scans shown in (b) and (c), and (e) height spectrogram (at 90° elevation) of W-Band SLDR from 08:30:00
 1196 UTC. The time and height frame of panels (b-e) is indicated by the black rectangle in (a).



1197

1198

1199

1200

1201

1202

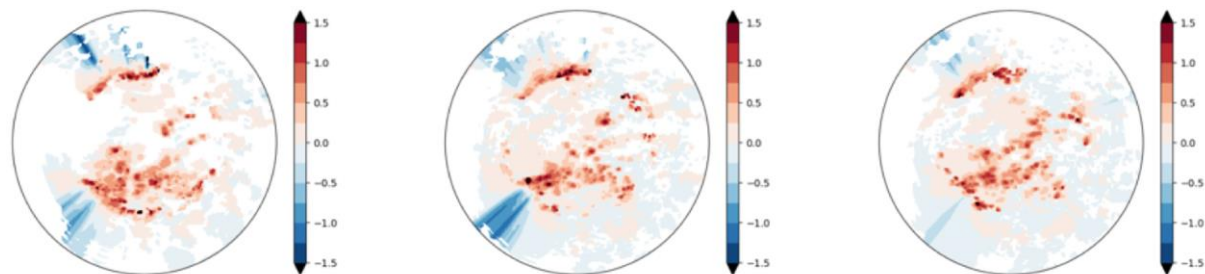
1203

1204

1205

Figure 5: Time-series of Convective Area Fraction (CAF) evolution (panel a) and reconstructed observed (panel b) and simulated/synthetic range-height-indicators (RHI) of horizontal reflectivity Z_H and differential reflectivity Z_{DR} (panels c and d). Synthetic RHIs are based on simulations for actual land-cover with different perturbations of CN and IN concentrations, where Cont-defIN indicates continental aerosol with default IN concentration and Mar-lowIN indicates maritime aerosol with low IN concentration. The gaps in the BoXPol-observed CAF time series are due to strong attenuation. The vertical grey bars (panel a) indicate the times at which the RHIs are compared.

1206

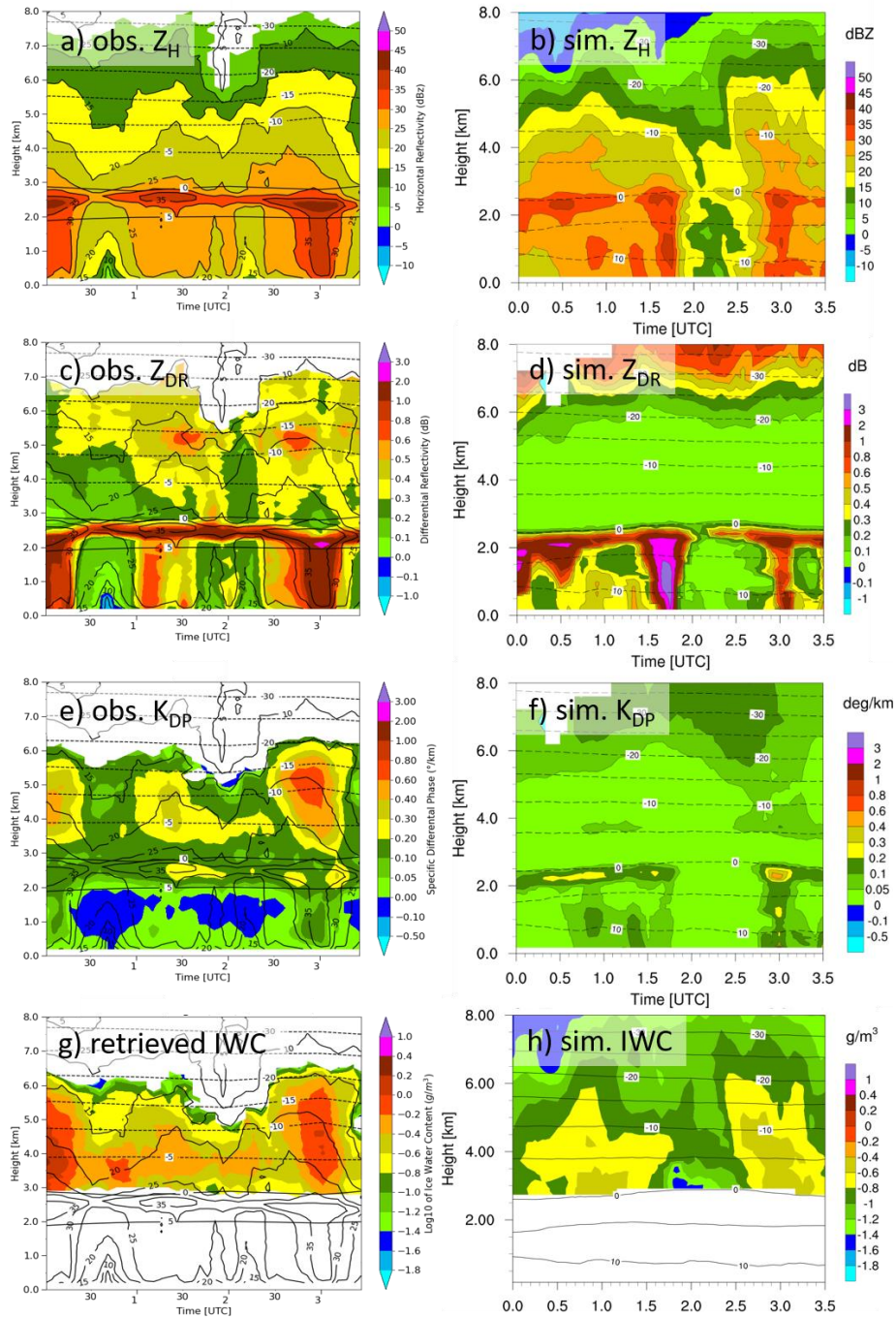


1207

1208

1209

Figure 6: Synthetic PPI of Z_{DR} at 0.5 deg elevation for the DWD radar site Neuheilenbach based on the analysis obtained for June 4 at 16:00 UTC by assimilation of radar reflectivity and using three different ways to specify the model error: large scale uncertainty (left), large plus unresolved scales uncertainty (middle) and in addition the use of the warm bubble approach (right).



1210

1211

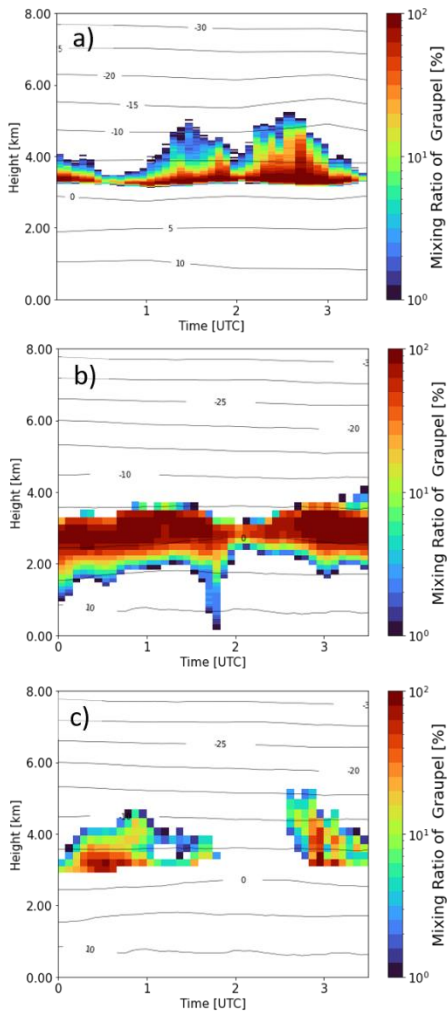
1212

1213

Figure 7: Quasi-vertical profiles (QVPs) of observed (left column) and simulated (right column) polarimetric radar variables horizontal reflectivity Z_H (panels a and b), differential reflectivity Z_{DR} (panels c and d), specific differential phase K_{DP} (panels e and f), together with radar-retrieved (panel g) and simulated ice water content (IWC, panel h). The QVPs show a stratiform rain event

1214 observed on 7 October 2014 between 0:00 and 3:30 UTC with the polarimetric X-band radar in Bonn, BoXPoL, and simulated with
1215 COSMO version 5.1 and the 2-moment cloud microphysics scheme.

1216



1217

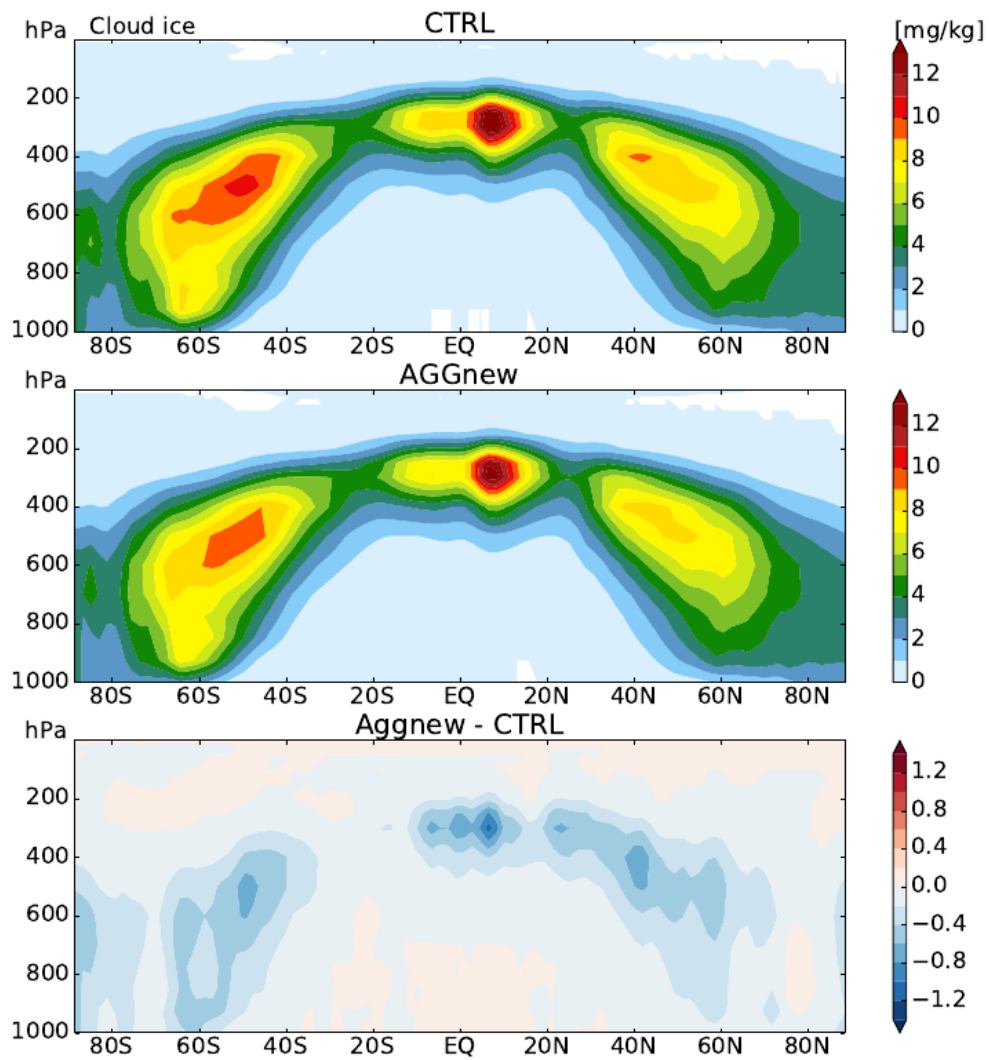
1218 **Figure 8: Retrieved and simulated graupel mixing ratios, defined as the percentage of graupel in the total hydrometeor mass, for**
1219 **the stratiform rain event shown in Fig. 7 (7 October 2014, 0:00-3:30 UTC). An advanced hydrometeor classification and**
1220 **quantification algorithm has been applied to polarimetric BoXPoL measurement (panel a) and to simulated radar variables based**
1221 **on COSMO simulations (panel c) and compared to the COSMO-simulated graupel mixing (panel b).**

1222

1223

1224

1225



1226

1227 **Figure 9:** Specific ice water, q_i [g kg^{-1}] as zonal, annual mean for (top) standard ICON GCM output, (middle) aggregation
1228 parameterization revised as stochastic parameterization drawing from the q_i subgrid-variability PDF, and (bottom) difference
1229 between the two.

1230

1231

1232

1233

1234